The anatomy of a long-lived fault system—structural and thermochronologic evidence for Laramide to Quaternary activity on the Tijeras fault, New Mexico

John C. Abbott[1], Laurel B. Goodwin[2], Shari A. Kelley[3], Stephen R. Maynard[4], and William C. McIntosh[5]

[1]*Science Applications International Corporation, 360 Bay Street, Suite 200, Augusta, GA, 30901*
[2]*Department of Geology and Geophysics, University of Wisconsin, Madison, WI 53706*
[3]*Department of Earth and Environmental Science, New Mexico Institute of Mining and Technology, Socorro, NM 87801*
[4]*Consulting Geologist, 4015 Carlisle NE, Suite E, Albuquerque, NM 87107*
[5]*New Mexico Bureau of Geology and Mineral Resources, New Mexico Institute of Mining and Technology, Socorro, NM 87801*

Abstract

Many previous workers have recognized that the Tijeras–Cañoncito fault system is a long-lived fault system. The number, timing, and kinematics of different deformation events, however, have been difficult to resolve due to a lack of piercing points and stratigraphic limitations. We propose a method for resolving the kinematics and minimum number of faulting events and use fission track and $^{40}Ar/^{39}Ar$ dating techniques together with geologic constraints to evaluate the timing of these events. Our approach is to use minor faults as a record of strain in the damage zone of the Tijeras fault and to assume that strain is compatible with fault slip. Thus, for example, the absence of evidence for crustal thickening in the damage zone is taken to indicate that the fault did not experience reverse motion.

This work indicates that fault-zone structural elements largely record dextral strike-slip motion with a component of north-side-down normal motion. This is the earliest faulting event, which thermochronologic and geologic constraints indicate initiated during the Laramide orogeny. The fault may have been reactivated during the transition in stress states between the Laramide orogeny and Rio Grande rifting and was definitely active during extension associated with the Rio Grande rift. Reactivation involved left-lateral strike-slip motion and, at least locally, further north-side-down normal movement.

Introduction

The history of faulting in New Mexico is, in large part, a history of reactivation. Elucidating the details of this history—in particular, seeing through the overprint of younger deformational events to determine the sense and magnitude of motion on older faults—is an ongoing challenge, critical to understanding the tectonic evolution of the southwestern United States. More specifically, if we consider the Rio Grande rift, two important points become evident. First, the major faults that accommodated extension within the north-trending rift do not all strike north; northeast and northwest-striking faults played a significant role in rift formation (Cordell 1978; Ramberg et al. 1978). Second, many of these faults or fault systems appear to record older deformation (e.g., Beck and Chapin 1994). In this paper, we explore the history of one such fault, the northeast-striking Tijeras fault, part of the Tijeras–Cañoncito fault system, from the earliest activity recorded by structures within the system to the present. This fault system was demonstrably active during rifting (e.g., Lisenbee et al. 1979; Abbott and Goodwin 1995; GRAM/William Lettis & Associates 1995; Kelson et al. 1999) and also has been a major element in most recent models for Laramide deformation in New Mexico (Cather 1999; Erslev 2001, and references therein). Until now, however, there has been no systematic investigation of kinematic data in the fault zone. In this paper we present new fault slickenside data, fission-track and $^{40}Ar/^{39}Ar$ ages of units cut by the fault, and descriptions of structural and sedimentological relationships that are key to understanding the deformational history of the fault system. These data, integrated with previous observations, demonstrate that both the large-scale geometry and internal structure of the fault system were established during the Late Cretaceous–early Tertiary Laramide orogeny. The fault system was reactivated in Oligocene time during a transition between Laramide tectonism and rifting and has accommodated extension in the Rio Grande rift into the Quaternary. There is no evidence for older deformation. Our work provides a context from which to view the many northeast-trending fault systems of New Mexico. In addition it suggests an approach to evaluating fault-zone kinematics in a long-lived fault system.

Previous studies—the Tijeras–Cañoncito fault system

Fault-zone geometry

The Tijeras–Cañoncito fault system (cf. Lisenbee et al. 1979) comprises a number of northeast-striking, subvertical faults, including the Tijeras, Gutierrez, San Lazarus, Los Angeles, and Lamy faults (Fig. 1). The system is regionally extensive; it has been mapped for more than 80 km, from Kirtland Air Force Base in the southwest (approximately 16 km southeast of Albuquerque) to the Cañoncito area in the northeast (roughly 20 km southeast of Santa Fe; Kelley 1954; Lisenbee et al. 1979). Russell and Snelson (1990, 1994) and May and Russell (1994) hypothesized that the existing Tijeras–Cañoncito fault system was utilized during Rio Grande rift extension as the Tijeras accommodation zone, which they suggest extends into the rift to the southwest. Recent studies, however, demonstrate that the Tijeras fault is connected to a north-striking splay of the Hubbell Spring normal fault zone on the eastern margin of the rift, and does not appear to be part of an accommodation zone related to rifting (Grauch 1999; Grauch et al. 1999; Maldonado et al. 1999). A left-stepping jog in the rift margin at this point shows up in aeromagnetic data, in which Precambrian granitic rocks north of the fault constitute a magnetic high; this geometry suggests that the Tijeras fault may have accommodated left-lateral slip during rift-related extension (Grauch 1999). In contrast, right-lateral separation of isostatic gravity anomalies across both the Tijeras fault and its inferred, along-strike extension on the west side of the Rio Grande rift (cf. Heywood 1992; Grauch et al. 1999) suggests that much of the fault system is buried by rift-related sediments and is no longer active. On the northeast end near Cañoncito, the fault system appears to link with the north-striking Picuris–

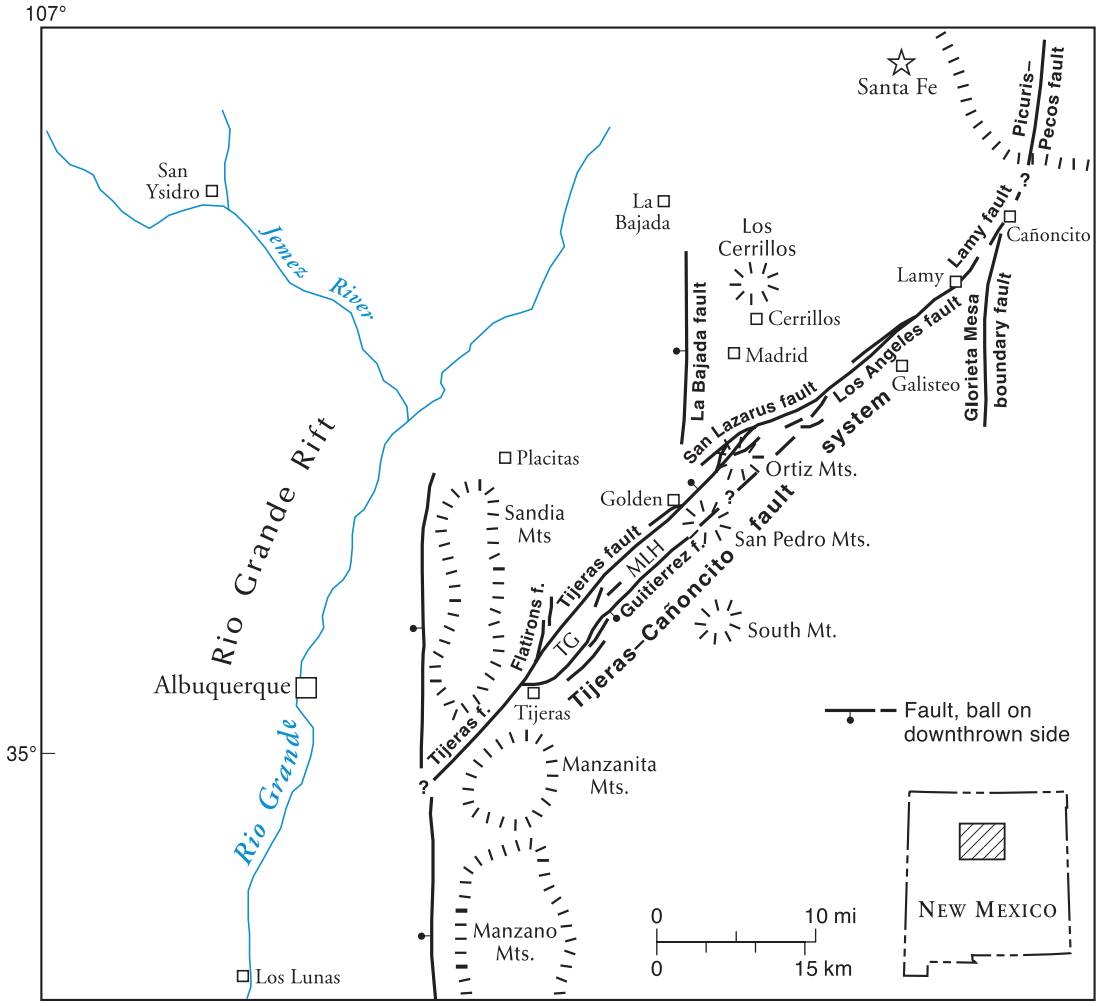

FIGURE 1—Location map and major structural elements of the Tijeras–Cañoncito fault system. **TG** = Tijeras graben; **MLH** = Monte Largo horst; and **f.** = fault.

Pecos fault system (Miller et al. 1963; Booth 1976; Ilg et al. 1997).

The Tijeras–Cañoncito fault system is characterized by sub-parallel faults, between which horsts and grabens are present, along much of its length. The largest of these structures are the Monte Largo horst and the Tijeras graben, which are located between the Gutierrez and Tijeras faults (Fig. 2). The horst and graben appear to be parts of a single fault block, rotated about a horizontal axis perpendicular to the faults (Kelley and Northrop 1975). Folds have been interpreted by some workers to have accompanied rotation of the block (Kelley and Northrop 1975) and by others to record contraction associated with transpression across the fault system (Ferguson et al. 1999).

A key exposure of the Tijeras fault near the village of Golden reveals a strongly but heterogeneously deformed zone more than 160 m wide, within which rocks of diverse lithologies and geologic ages are locally tectonically mixed (Abbott and Goodwin 1995). Within this tectonic mélange, lithologically distinct blocks are separated by east-northeast-striking, steeply dipping faults, which are oblique to the northeast-striking Tijeras fault.

Movement history

Despite decades of interest, understanding of the Tijeras–Cañoncito fault system is surprisingly limited. This is in part because the deformational history of the fault system has generally been only a peripheral topic in studies of the geologic history of adjacent rocks. In addition, although the fault system clearly has a complex history of recurrent movement, no piercing points are available to constrain the magnitude of net displacement, let alone displacement for any given episode of movement. The sole constraints on net slip are inferred from geophysical data. Isostatic gravity anomalies exhibit ~ 5.5 km of right-lateral separation across the Tijeras fault and ~ 13.5 km of right-lateral separation across the inferred extension of the fault system on the west side of the rift (cf. Heywood 1992; Grauch et al. 1999). In contrast, aeromagnetic anomalies show 2.4 km of left-lateral separation where the Tijeras fault intersects the eastern margin of the rift and there is a jog in the rift margin (Grauch 1999).

A number of workers have documented evidence that might be used to constrain the timing and sense of motion on the Tijeras fault, which is presented in chronologic order in the following paragraphs. The oldest rocks in the vicinity of the Tijeras–Cañoncito fault system are exposed in the Monte Largo horst and in Tijeras Canyon (Fig. 2). In Tijeras Canyon the Tijeras fault juxtaposes different Proterozoic lithologies. On the southeast side of the fault is the Tijeras greenstone, a ca. 1.68 Ga sequence of metavolcanic and metasedimentary rocks (Bruns 1959; Condie 1982; Connolly 1981, 1982; S. Bowring in Nelson and DePaolo 1984). On the northwest side of the fault is the Cibola gneiss, a ca. 1.65 Ga granite deformed under amphibolite-facies conditions (Vernon 1986; Mawer et al. 1989; Kirby et al. 1995a,b; Dan

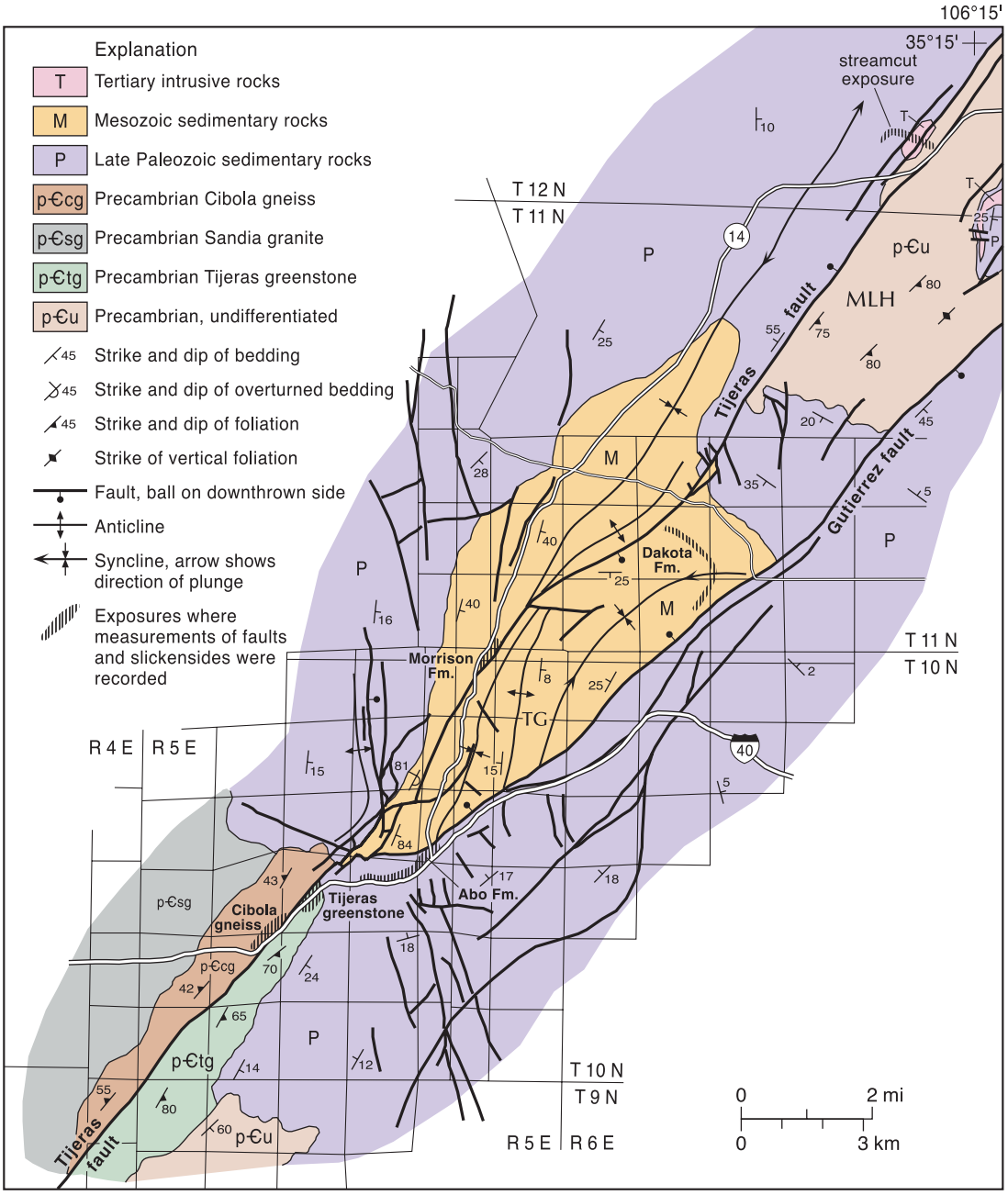

FIGURE 2—Major structural elements of the Tijeras–Cañoncito fault system near Tijeras graben (**TG**) and Monte Largo horst (**MLH**). Modified from Kelley and Northrop (1975). Exposures in which minor faults were measured are marked and labeled for correlation with Figures 4 and 5. Fission-track sample TIJ2 was obtained from marked exposure of Cibola gneiss on I–40.

Unruh, unpublished U-Pb zircon date). Connolly (1982), Kirby et al. (1995b), and Timmons et al. (1995) demonstrated that the Tijeras–Cañoncito fault system crosscuts a metamorphic aureole surrounding the Sandia granite, indicating that it is younger than the ca. 1.42 Ga intrusion. However, the morphology and extent of both the pluton and its aureole are poorly constrained, so that it is not possible to deduce the sense of fault movement from these data. Based on quartz veins, simple pegmatite dikes, and minor aplite dikes in the Tijeras greenstone, which were interpreted to form an en echelon array, Lisenbee et al. (1979) and Connolly (1982) suggested that the initial movement on the Tijeras fault was left lateral and coincident with intrusion of the Sandia granite.

An understanding of the geologic history of north-central New Mexico between the Middle Proterozoic and the late Paleozoic is limited by the absence of rocks from this time interval in this area. The next oldest rocks adjacent to the Tijeras–Cañoncito fault system are late Paleozoic in age. Lisenbee et al. (1979) noted that the Pennsylvanian Sandia Formation is generally thicker and coarser on the northwest side of the Tijeras fault and attributed this sedimentation pattern to late Paleozoic, south-side-up motion on the fault system.

North-side-down throw on the Guiterrez fault subsequent to deposition of the Upper Cretaceous Mesaverde Group is locally as great as 1,500 m (Kelley and Northrop, 1975). Stearns (1953) described both horizontal and vertical

separations across the fault system in Cretaceous and Tertiary rocks near Galisteo Creek. Several workers (Kelley and Northrop 1975; Lisenbee et al. 1979; Chapin and Cather 1981) interpreted folds oblique to the fault system to record right-lateral strike-slip motion in the Tertiary. Abbott and Goodwin (1995) interpreted minor faults within a tectonic mélange in the Tijeras fault zone as Riedel shears that record right-lateral strike-slip movement based on their orientation with respect to the main fault (cf. Tchalenko 1970). Ferguson et al. (1999) interpreted structures in the Tijeras–Cañoncito fault system, including the Tijeras and Gutierrez faults, as recording dextral transpression in Laramide time. Ferguson (1999) subsequently suggested that only the Gutierrez fault was active during the Laramide orogeny, and that the Tijeras fault initiated in the Miocene as a left-lateral strike-slip fault. Pronounced stratigraphic thickening and highly variable paleocurrent directions in the strata of the Paleogene Galisteo Basin immediately adjacent to the Tijeras–Cañoncito fault system indicate that the fault system was active in the Paleogene and controlled subsidence and sedimentation to the northwest (Cather 1992; Abbott et al. 1995). Because the southeast block was not emergent, the maximum displacement magnitude of the Paleogene dip-slip component on the Tijeras–Cañoncito fault system is constrained to approximately the thickness of the strata of the Galisteo Basin (approximately 1,300 m, northwest-side-down; Abbott et al. 1995).

A period of widespread volcanic and igneous activity followed the Laramide orogeny (Stearns 1953; Cather 1989). A shallow intrusive center, the San Pedro–Ortiz porphyry belt, was emplaced in and around the Tijeras–Cañoncito fault system in the Oligocene (Bachman and Mehnert 1978; Woodward 1984; Kay 1986; Maynard et al. 1990; Maynard et al. 1991; Sauer 1999). Mineral deposits in the Ortiz Mountains are localized along the Tijeras–Cañoncito fault system, and a genetic relationship between faulting and mineralization has been demonstrated by a number of workers (Woodward 1984; Kay 1986; Maynard et al. 1990; Maynard et al. 1991). Maynard et al. (1990) showed that intrusion and mineralization were broadly contemporaneous with faulting, and that a K-Ar date on hornblende from an igneous intrusive on the west side of the Ortiz Mountains constrains the timing of mid-Tertiary movement on this portion of the Tijeras–Cañoncito fault system to 30–34 Ma (early Oligocene).

Ferguson et al. (1999) described and mapped high-angle, north- to northwest-striking faults with small left-lateral separations and east-striking apparently dextral faults adjacent to the Tijeras fault. They interpreted these structures as synthetic and antithetic Riedel shears, respectively, and proposed that they record reactivation of the fault during mid-Tertiary left-lateral strike-slip. However, synthetic Riedel shears typically form at a low angle, and antithetic shears at a high angle, to the primary fault surface (Riedel 1929; Tchalenko 1970), exactly the opposite of the relationship described above. This fault pattern therefore requires additional explanation. Ferguson (1999) subsequently suggested that the Tijeras fault initiated as a mid-Tertiary left-lateral strike-slip structure that overprinted the Gutierrez fault and associated structures.

In Tijeras Canyon the Tijeras fault juxtaposes Proterozoic Tijeras greenstone and colluvium (Lisenbee et al. 1979) of probable Pleistocene age (B. Harrison and D. Love, personal comm. 1994). Separation on this fault is northwest-side-down. Near the village of Golden (Fig. 1) Quaternary activity on the Tijeras fault is illustrated by relationships between faulting and sedimentation (Abbott and Goodwin 1995). A streamcut exposes a strand of the Tijeras fault that incorporated Quaternary carbonate-rich mottled clay and pebbly gravel into the fault zone, but is overlain by Quaternary imbricated gravel. The southeast-side-down separation of this fault is opposite that of both the previously described Quaternary fault in Tijeras Canyon (Lisenbee et al. 1979) and a strand of the Tijeras fault just a kilometer to the north, probably reflecting significant lateral motion (Kelson et al. 1999). Abbott and Goodwin (1995) suggested that Neogene motion on the Tijeras fault was left-lateral based on minor fault kinematics; Kelson et al. (1999) agreed, citing 30 m of left-lateral deflection of an unnamed arroyo. Previous workers have also suggested that the Tijeras–Cañoncito fault system served as a transfer fault during rift-related extension. Transfer faults typically exhibit variations in magnitude and sense of motion along strike; Lisenbee and Woodward (1995) proposed that the sense of slip changes along strike within the Tijeras–Cañoncito fault system. Southwest of the normal La Bajada fault (Fig. 1), they suggested that net extension is greater on the southeast side of the fault system, resulting in left slip. To the northeast, they suggested that extension is greater on the northwest side of the fault system, resulting in right slip. Machette et al. (1998) noted that there is no documented evidence of Quaternary activity on the Tijeras–Cañoncito fault system northeast of the La Bajada fault.

Additional evidence for Quaternary activity on the Tijeras–Cañoncito fault system is found in the Holocene sediments of the Rio Grande rift. Gibbons (1990) suggested that the drainage system from Tijeras Canyon was disrupted by Holocene interaction between the Tijeras and Hubbell Spring faults, and Machette (1982) surveyed Holocene scarps that may be southwestern continuations of the Tijeras fault. It is not known whether there has been any surface rupture on the fault system in historical time, though several earthquakes have been recorded near or on the Tijeras fault in the past several decades (Sanford et al. 1991). The largest one (M.M. VI) occurred on November 6, 1947, near Tijeras and Cedar Crest (Kelley and Northrop 1975).

In summary most workers agree that structures associated with the Tijeras–Cañoncito fault system record at least one episode of left-lateral strike-slip and that activity on the fault continued into the Quaternary. The timing of initiation of faulting, however, is debated, as is the timing, significance, and location within the fault system of right-lateral strike-slip motion. The length of the fault system and the width and magnitude of deformation within the Tijeras fault zone, however, all suggest significant displacement on the fault system, consistent with the offset gravity anomalies.

Principles and methods of fault-zone kinematic analysis

As mentioned above, there are no piercing points to constrain net slip on the Tijeras–Cañoncito fault system. The deformation history of the system must therefore be inferred from the character, orientation, and distribution of major and minor structures in the fault zone, stratigraphic separation, and sedimentologic data. Previous work on the San Andreas fault system suggests an approach to optimizing the information obtained from subsidiary faults and folds, which we have employed in this study. The background required to understand this approach is provided in the following paragraphs.

Faults are typically surrounded by zones of damage, within which minor structures overprint regional structures. The width of a damage zone is determined by the density of fault-zone structures, which decreases with distance from a given fault; damage-zone width may vary depending on which structures are used to define it. For example the width of the damage zone around the Punchbowl fault (a strand of the San Andreas fault system) defined by the

extent of fault-related microfractures is more than triple that defined by macroscopic shear fractures and minor faults (Wilson 1999). In this paper, we consider the damage zone around the Tijeras fault as defined by the distribution of macroscopic minor faults and fractures, but also consider fractures in outcrops outside the damage zone proper (outcrops studied are shown in Fig. 2).

Patterns of deformation in the vicinity of the San Andreas fault reflect deformation partitioning (see reviews by Teyssier et al. 1995 and Tavernelli 1998). The fault itself accommodates right-lateral strike-slip motion, but structures to the southwest and northeast record fault-perpendicular shortening. Minor fault data collected west of the San Andreas fault (Tavarnelli 1998) and within the damage zone of the Punchbowl fault, a dormant strand of the San Andreas that accommodated approximately 20 km of right-lateral strike-slip before exhumation (Fig. 3; Chester and Logan 1987), record this partitioning. Structures within the northern Salinian block, west of the San Andreas fault, include folds that typically trend subparallel to the fault and plunge shallowly to moderately northwest or (less commonly) southeast, and northwest-striking thrust faults that dip both southwest and northeast (Fig. 3A; Tavarnelli 1998). The data shown in Figure 3A are typical of 127 faults studied; most of these data were apparently collected more than 1 km from the major faults of the San Andreas system. They record shortening at nearly right angles to the San Andreas fault. The inferred maximum principal stress would also be at a high angle to the fault.

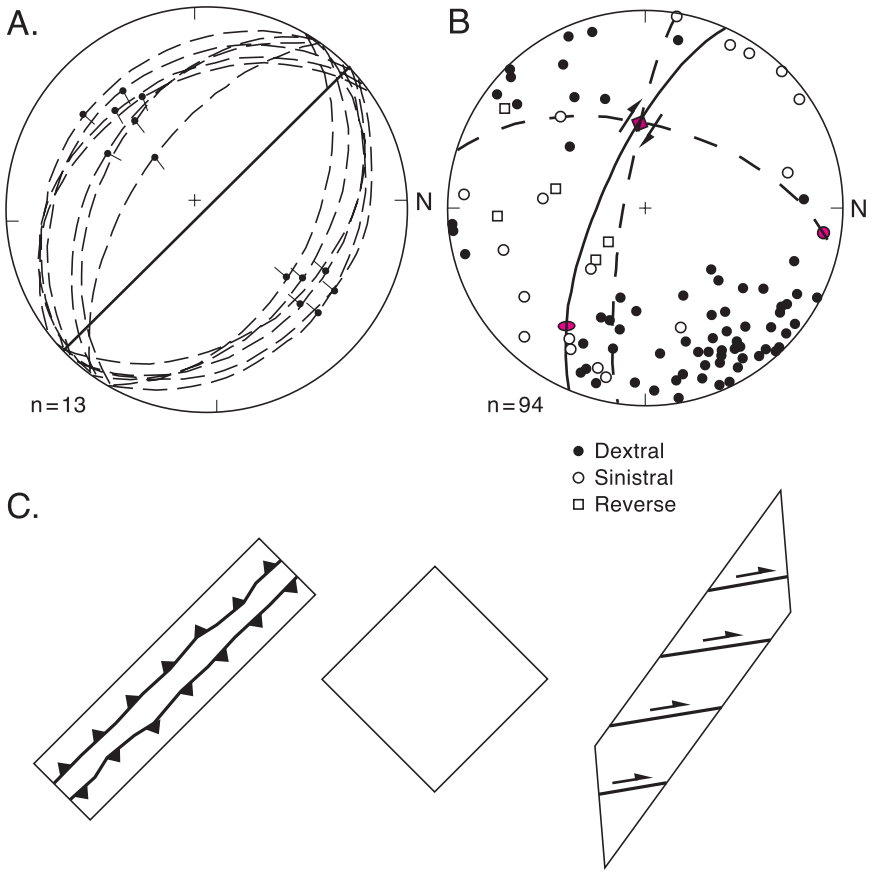

FIGURE 3—Lower hemisphere, equal area net plots of minor faults associated with the San Andreas fault system. Figures have been rotated to facilitate comparison with data from the Tijeras fault. (**A**) Faults from Bodega Head, Salinian block, west of the San Andreas Fault, showing representative orientations of thrust faults (dashed lines) and slickenside striae (solid circles with tails indicating slip directions). The trace of the San Andreas fault is shown as a solid line. After Tavernelli (1998). (**B**) Poles to minor faults within the damage zone of the Punchbowl fault; key indicates fault type. Punchbowl fault trace is shown as solid line. Dashed lines separate fields of dextral and sinistral strike-slip faults. Red square is the Punchbowl fault B-axis inferred from minor faults and folds. Red ellipse is the inferred slip direction; red circle is the inferred maximum principal stress orientation. Note that this is a dominantly dextral strike-slip fault with a reverse component of movement. Modified from Chester and Logan (1987). (**C**) Differences in change of shape of area of damage zone (initial unfaulted square shown in center) produced by minor thrust faults parallel to the main slip surface (left) and dextral strike-slip faults oblique to the main slip surface (right). See text for further explanation.

In contrast the Punchbowl damage zone defined by the distribution of macroscopic minor faults and fractures, which varies in width but extends roughly 30 m from the main fault, is dominated by minor dextral strike-slip faults that strike oblique to the main fault (Fig. 3B). The orientation and slip sense of the latter faults indicates that they may have originated as Riedel shears (cf. Riedel 1929). Similar damage-zone fault patterns are exhibited by a number of faults in the San Andreas system (e.g., Ghisetti 2000). Ghisetti (2000) noted that small-scale faults with similar orientations and mechanisms to adjacent master faults are rare. Given typical patterns of shear fractures associated with faults (e.g., Riedel 1929; Tchalenko 1970), one might anticipate this lack of correspondence. The fault patterns and associated strain in damage zones should, however, vary in a consistent and predictable fashion with the shear sense of the master fault.

The Punchbowl fault is located in a bend in the San Andreas fault system, so it has accommodated a component of reverse slip in addition to dextral shear. The fault dips steeply to the southwest, rather than vertically, and vertical separation records the reverse component of movement. The fault B-axis (the intermediate principal strain axis) has been determined from fold and minor fault data, and the slip direction on the Punchbowl fault has been inferred from that axis (Fig. 3B; Chester and Logan 1987). Fold axes used in this evaluation were determined from folded strata up to 1 km from the fault. The inferred maximum principal stress is oriented at a high angle to the fault plane, as in the previous example. Previous workers have suggested that this stress orientation reflects the mechanically weak nature of the fault zone (e.g., Mount and Suppe 1987; Zoback et al. 1987).

The inferred orientation of the maximum principal stress is therefore close to perpendicular to the San Andreas fault both within and outside the damage zone in the areas studied. Patterns of structures, however, are distinctly different and record different strain in the two areas. These differences are illustrated in Figure 3C. If we consider an initial cubic volume of rock, illustrated in two dimensions as a square, the shape change associated with deformation shown in 3A will be distinctly different from that in 3B. Conjugate thrust faults will produce shortening roughly perpendicular to the fault, accompanied by vertical exten-

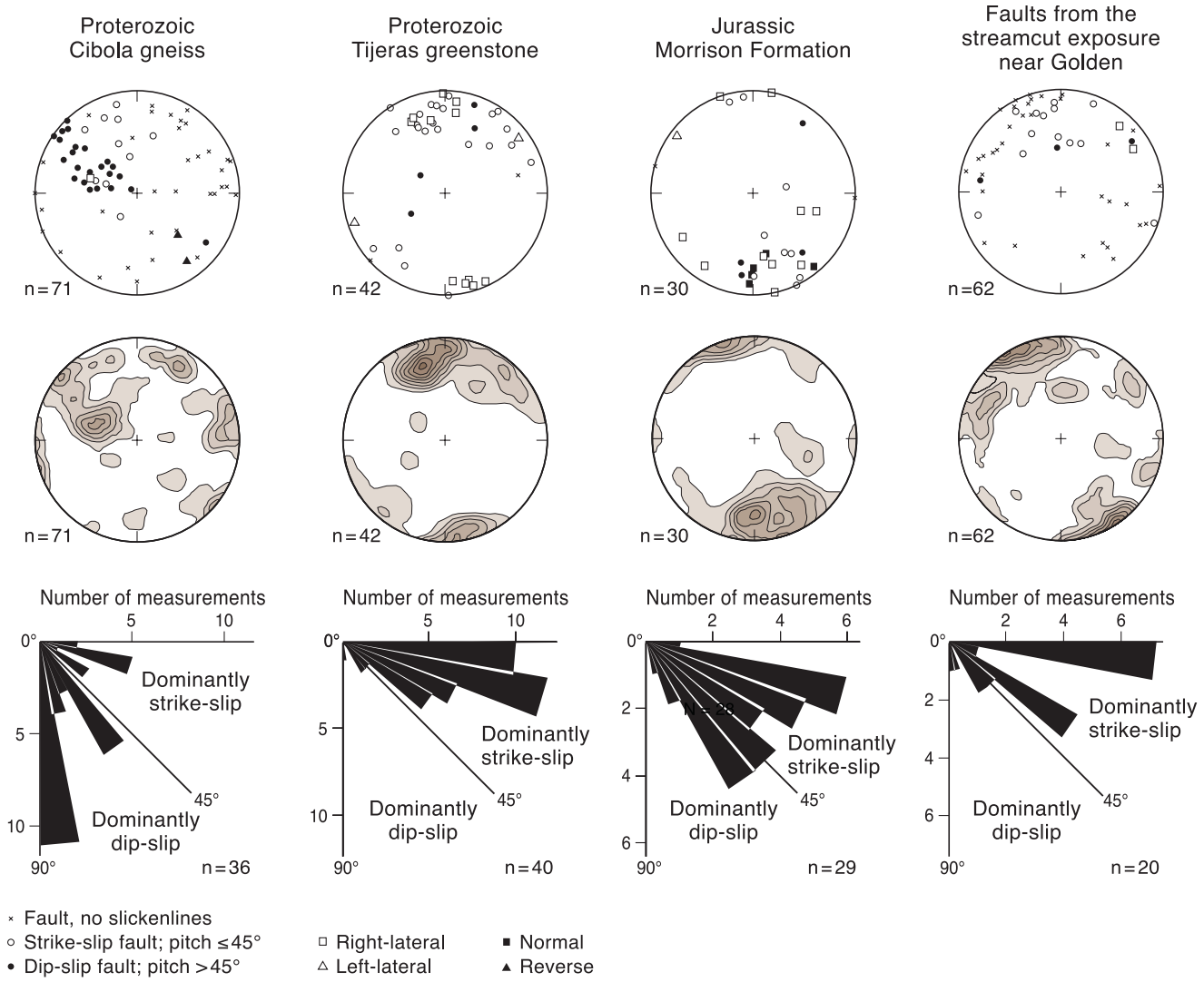

FIGURE 4—Minor fault and slickenline data from the Tijeras fault. From left to right, areas are located from southwest to northeast along the fault; exact locations shown on Figure 2. The Golden streamcut exposure includes rocks of Precambrian, Pennsylvanian, Permian, and Oligocene age as well as Quaternary surficial deposits. **Top row**: Equal area, lower hemisphere projection of poles to minor faults. Dominant component of slip (e.g., dip-slip or strike-slip) and, where it can be determined, sense of slip on each slickenside are indicated. **Center row**: Poles to faults contoured in multiples of uniform distribution (m.u.d.). White is less than one m.u.d., each subsequent contour represents an increase in one m.u.d. The data are plotted and contoured using the program and method of Starkey (1977). **Bottom row**: Pitches of slickenlines from slickenside surfaces. Each petal is 10°. Note that the scale varies from left to right.

sion. The strikes of the thrust faults will all be similar. In contrast, a damage zone dominated by strike-slip faults will result in shortening at a high angle to the main fault and subhorizontal extension nearly parallel to fault strike. In the case of the Punchbowl fault, the structures in the damage zone, vertical separation, and folds up to 1 km from the fault collectively record slip sense on the main fault. The minor faults record dextral shear on the main fault, vertical separation records the reverse component of slip, and the fold axes and faults can be used to determine the orientation of the slip vector, as described above. Slip sense along the San Andreas fault cannot, however, be inferred from the maximum principal stress orientation.

These data also suggest a mechanism for evaluating deformation partitioning. If there is significant strain partitioning, structures outside the fault zone will record different strain than those within the damage zone, but the inferred maximum principal stress orientation will be the same in both areas.

The approach taken in this study is to evaluate structures within the damage zone of the Tijeras fault and in other structural locations within the fault system in order to constrain fault-zone kinematics by the method suggested above. We integrate the results of this study with thermochronologic and other geologic data in order to constrain the kinematic history of the system, then compare our results with Erslev's (2001) regional study of stress orientations in northern New Mexico to evaluate the possibility of strain partitioning.

The kinematic history of the Tijeras–Cañoncito fault system

Minor faults

The orientations of 289 minor faults were measured from outcrops shown in Figure 2, which were chosen for both their locations and quality of exposures, in units ranging from Proterozoic to Quaternary in age (Figs. 4, 5). Of these, 189 have slickensides with slickenlines. The sense of slip was determined from secondary fractures or slickenfibers

on 48 of these slickensides, using criteria described by Petit (1987). The measured faults are grouped by geographic location, which also generally corresponds to grouping by geologic age of the unit cut by the faults (Fig. 2). Measurements were taken from the damage zone adjacent to the Tijeras fault, within the Tijeras graben, and from an area adjacent to the east-striking fault that bounds the southern end of the graben. Several distinct populations of slickensides are evident, few of which are parallel to the fault system (~ 045°, 90°). Slickenlines vary in pitch from 0° (pure strike-slip) to 90° (pure dip-slip). The relative amounts of strike-slip and dip-slip motion, however, vary with position in the fault system. The patterns exhibited by the minor faults are striking in their consistency. East-northeast-striking faults dominate the population along the Tijeras fault, where the majority of slickenlines on faults that border the Tijeras fault record dominantly strike-slip movement (Fig. 4). In contrast, faults from the other two regions are largely dip-slip structures (Fig. 5). Details of the minor fault record from each of the three portions of the fault system are discussed in the following sections. Additional information regarding the orientation of bedding and other structures at each site, character of mineralization of each fracture, etc., can be found in Abbott (1995).

Damage zone of the Tijeras fault

The largest population of minor faults strikes east-northeast, dips subvertically, and has slickenlines that vary in pitch with position in the fault system. In most exposures adjacent to the Tijeras fault, slickenlines typically pitch much less than 45° (Figs. 4, 6A). Northwest of the Tijeras graben (in the Jurassic Morrison Formation), however, there is also a significant population of slickenlines that pitches between 40° and 60° (Fig. 4). East-northeast-striking faults that cut the Morrison Formation record variable components of right-lateral strike-slip and normal, down-to-the-north movement. Some of these faults are dominantly strike-slip whereas others are dominantly normal (Fig. 4). Twenty slickensides measured adjacent to the Tijeras fault record right-lateral motion; of these, five have a significant normal component of movement and one records a significant reverse component of slip. A single slickenside records normal movement with a left-lateral component. Most of these faults cut rocks Cretaceous and older in age; however, in the streamcut exposure near Golden, six faults of this orientation cut an Oligocene porphyry, and one juxtaposes the porphyry and Quaternary(?) sediments. In sec. 15 T10N R5E detailed mapping has demonstrated right-lateral separation of steeply dipping Mesozoic strata across map-scale, east-northeast-striking, high-angle faults (Fig. 7).

A second population, composed of subvertical, northwest-striking faults oriented roughly perpendicular to the fault system, is evident throughout the area (Fig. 4). Slickenlines on all of these faults record a component of strike-slip motion, although three are dominantly dip-slip faults. Four slickenside surfaces in this population exhibit secondary fractures that record right-lateral strike-slip motion, two of which record a significant component of normal movement. Conversely, secondary fractures on one slickenside, and slickenfibers on another slickenside in the Tijeras greenstone, both record left-lateral strike-slip movement. The pitch of slickenlines on both of these is less than or equal to 5°.

North- and north-northeast-striking subvertical faults are evident in all of the exposures along the Tijeras fault (Figs. 4, 5). In most cases, these are high to low-angle dip-slip faults, but the sense of slip cannot be determined. However, two slickensides located in the Morrison Formation record right-lateral strike-slip motion. Both are relatively low-angle

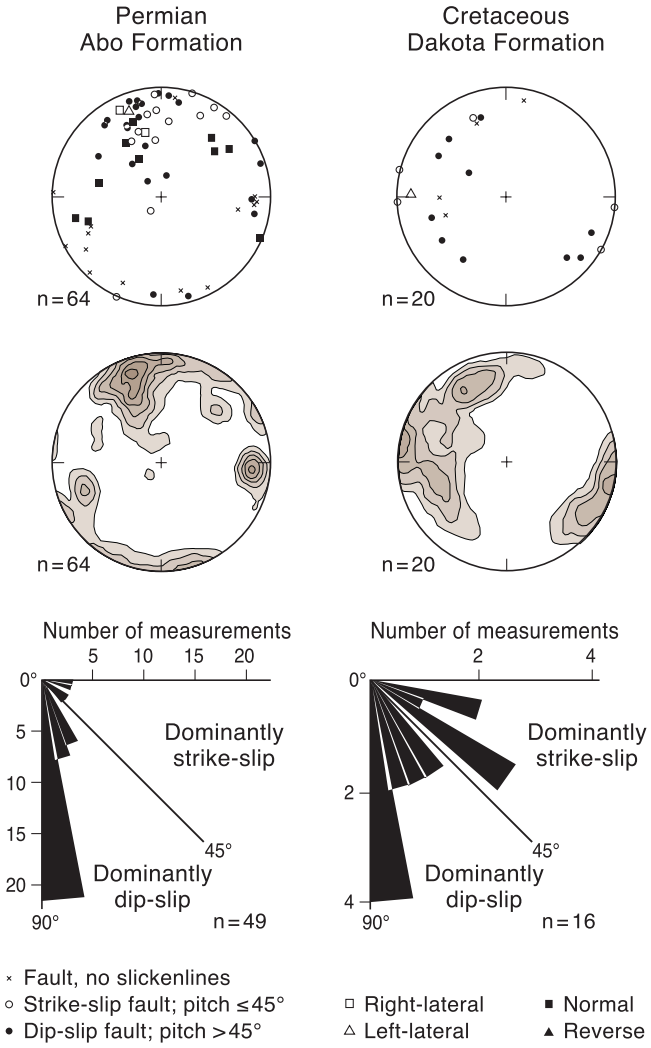

FIGURE 5—Minor fault and slickenline data from the vicinity of the Tijeras graben. Faults in the Abo Formation were measured adjacent to the southwest margin of the graben; faults in the Dakota Sandstone were examined within the graben. Locations of areas studied shown in Figure 2. **Top row**: Equal area, lower hemisphere projection of poles to minor faults. Dominant component of slip (e.g., dip-slip or strike-slip) and, where it can be determined, sense of slip on each slickenside are indicated. **Center row**: Poles to faults contoured as in Figure 4. **Bottom row**: Pitches of slickenlines from slickenside surfaces. Each petal is 10°. Note that the scale varies from left to right.

faults, which dip between 40° and 53° W. In the Cibola gneiss and the Morrison Formation, faults that strike northeast to north-northeast and dip steeply to moderately to the southeast and east-southeast have slickenlines that generally record a dominant component of dip-slip motion, though some pitch between 20° and 30°. Kinematic indicators on two of the latter record dominantly right-lateral strike-slip motion; one records dominantly left-lateral strike-slip motion. Each of these records a measurable component of normal movement. Secondary fractures on two dip-slip slickensides record normal displacement. Two northeast-striking, northwest-dipping faults with slickensides in the Cibola gneiss are notable because they are the only two measured slickensides in the fault system that record a dominant component of reverse motion.

Southwestern margin of the Tijeras graben

Near the southwestern margin of the Tijeras graben (Fig. 5,

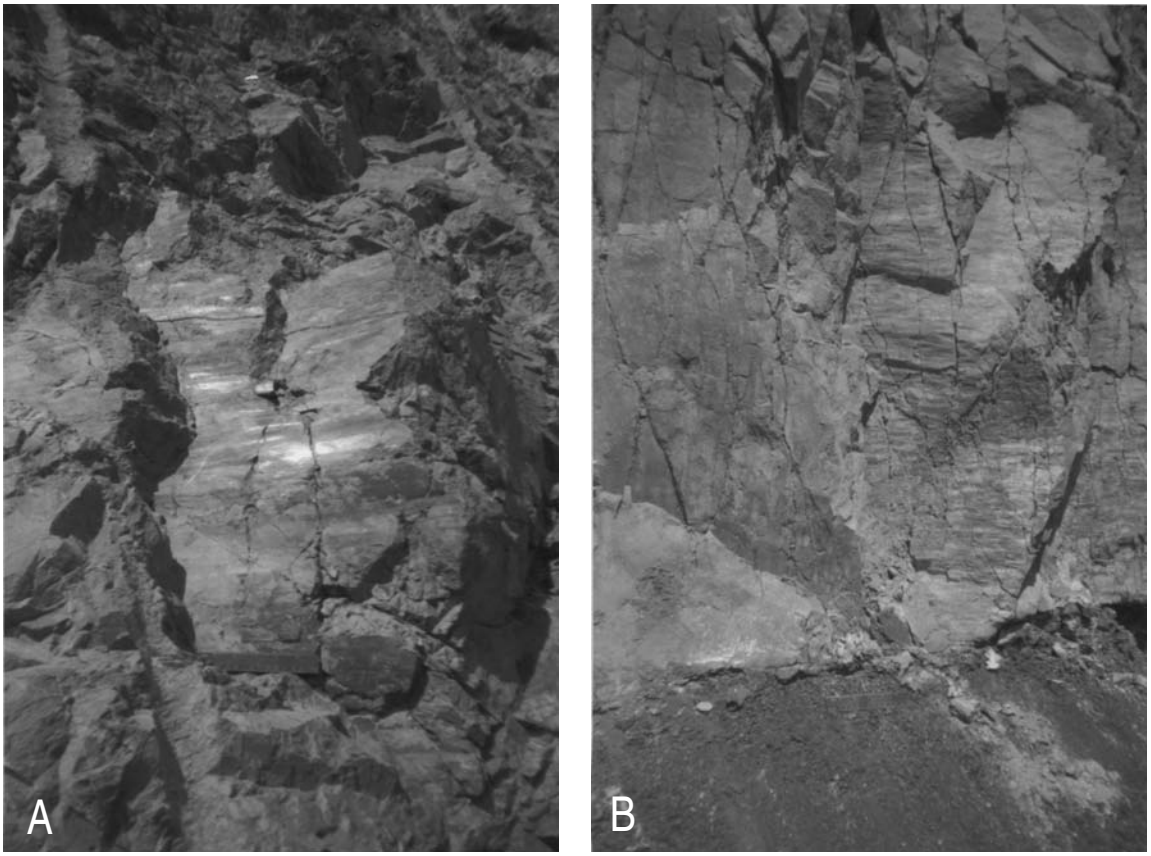

FIGURE 6—**A:** East-northeast-striking fault slickenside in the Tijeras greenstone with well developed horizontal slickenside striae indicating strike-slip motion. 15-cm ruler for scale. **B:** Two fault surfaces in the Abo Formation of similar orientation that record different kinematic histories. The fault on the right has well developed subhorizontal slickenside striae, indicating strike-slip movement. The fault on the left has well developed down-dip slickenside striae, indicating dip-slip motion. Faults strike east-northeast.

Permian Abo Formation), slickenlines on east-northeast-striking slickensides record dominantly dip-slip motion, though strike-slip faults are locally evident (Fig. 6B). Four of the five faults in this population with kinematic indicators record normal displacement; one records dominantly left-lateral motion with a reverse component.

The pitch of slickenlines on northwest-striking faults varies from 60° to 80°. Slickenfibers and/or secondary fractures on three of these slickensides record a dominant component of normal motion. A third population of north- and north-northeast-striking subvertical faults includes four slickensides that also record normal movement.

Within the Tijeras graben

Within the Tijeras graben, steeply dipping minor faults in the Dakota Sandstone exhibit the same strike populations as faults elsewhere in the system (Figs. 4, 5). Most of these faults are dip-slip structures, although six are dominantly strike-slip faults and one north-striking slickenside exhibits secondary fractures that record left-lateral strike-slip motion.

Discussion—analysis of minor faults

A critical concern in analyzing minor faults and shear fractures from the damage zone of a larger fault is the possibility of rotation of fault-bounded blocks. Rotation of faults and fractures will result in a wide variety of orientations that do not reflect either stress or strain. An apparently random array of fault orientations therefore is characteristic of areas of significant block rotation. Minor faults from both the damage zone of the Tijeras fault and the Tijeras graben, however, exhibit strikingly regular patterns (Figs. 4,5), suggesting that the faults did not experience substantial rotation subsequent to formation. We therefore conclude that these faults provide an accurate record of the deformation history. As explained earlier, minor faults in the damage zone should generally be oriented differently than the adjacent main fault, and normal, reverse, and both left- and right-lateral strike-slip faults may be present in a given fault zone regardless of the sense of slip of the main fault (cf. Ghisetti 2000). Despite this variability, the minor fault population will provide information about the kinematic history of the main fault in the orientations of the different fault types and slickenlines, as well as in the shortening and extension directions they record (e.g., Fig. 3).

The maximum shortening and extension (strain) directions were determined for each minor fault using FaultKin v. 3.8.3 (Allmendinger et al. 1992), which uses a fault plane, lineation, and slip sense to create a fault-plane solution. The principal shortening and extension directions are estimated by bisecting the angle between the nodal planes of the fault plane solution (Marrett and Allmendinger 1990). It is important to note that: 1) these calculations do not constrain the magnitude of strain and 2) unlike estimations of stress orientations, these calculations do not require assumptions about either the mechanical properties or the deformational history of the rocks. The principal strain orientations for the most recent movement on a given fault can be determined whether or not it is a reactivated surface.

The principal strain directions, determined from all but

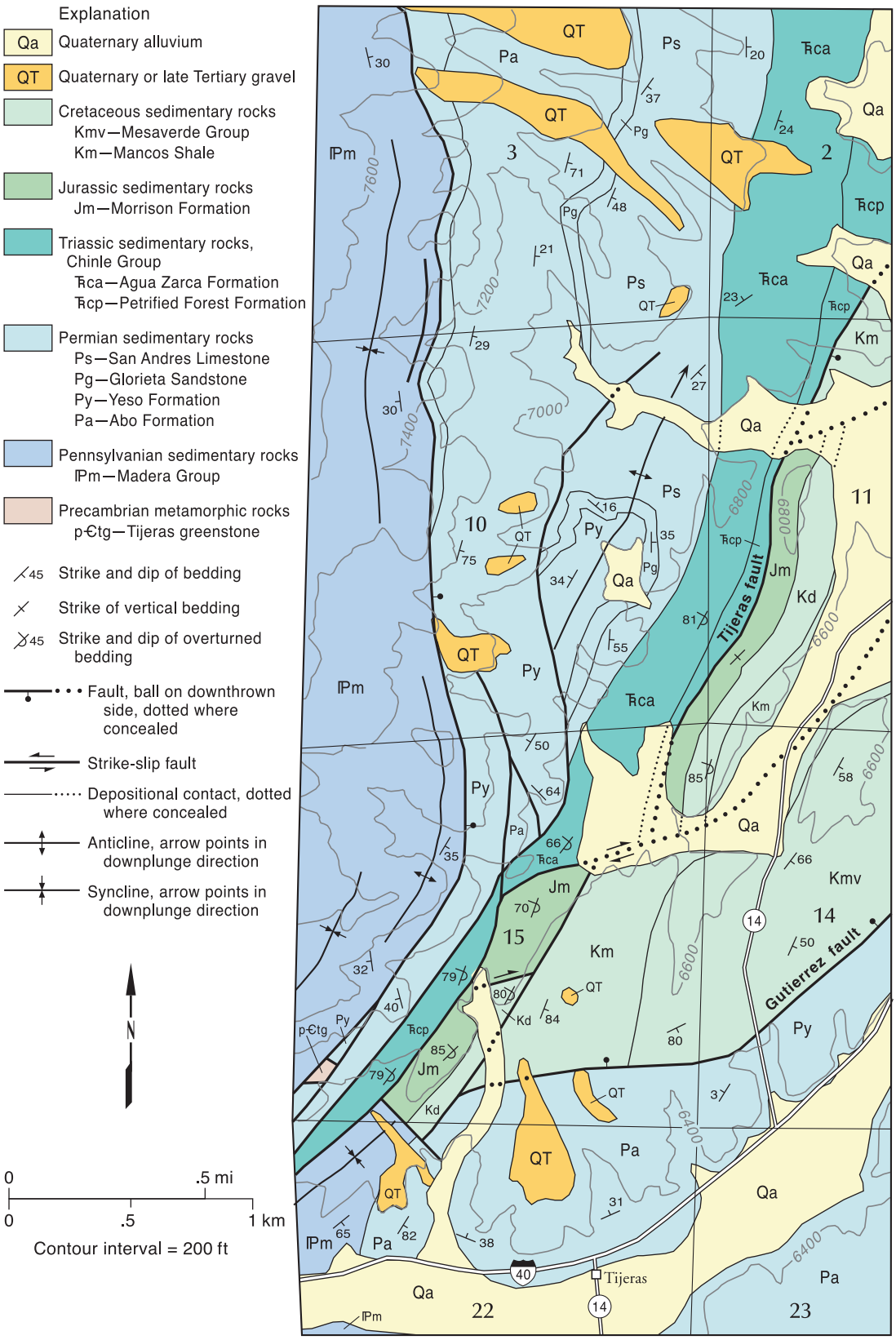

FIGURE 7— Simplified geologic map of the northeastern part of the Tijeras 7.5′ quadrangle near the southwestern end of Tijeras graben. Note right-lateral separations and deflection of steeply dipping Mesozoic sedimentary rocks across east-northeast-striking faults (Karlstrom et al. 1994).

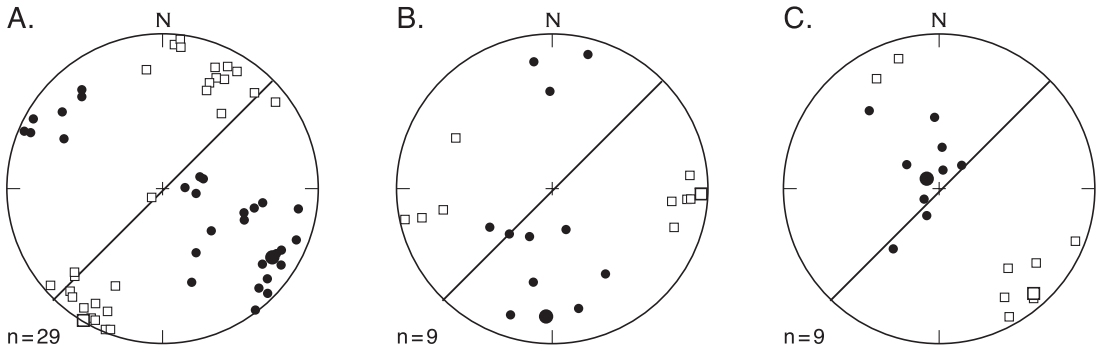

FIGURE 8—Results of strain analyses of minor faults from the Tijeras–Cañoncito fault system, plotted on lower hemisphere equal area nets. Shortening directions shown with solid circles; the mean shortening direction in each diagram is a large solid circle. Extension directions are shown by open squares; the mean extension direction in each plot is a large open square. Numbers of faults are given for each plot. Trace of typical Tijeras fault orientation (045, 90) is shown as a solid line. Extension and shortening directions were determined from faults from: (**A**) the Cibola gneiss, Tijeras Greenstone, and Abo, Morrison, and Dakota Formations, (**B**) the Cibola gneiss and Abo and Morrison Formations, and (**C**) the Golden site and Abo and Morrison Formations.

two of the fault planes measured, fall into three distinct groups on the basis of orientation (Fig. 8). Perhaps the most notable feature of these groups is that they all exhibit subhorizontal extension; only two faults of forty-seven (Fig. 8A) record steeply plunging extension directions. These two faults and associated slickenlines, both in the Cibola gneiss, have orientations that are anomalous with regard to all other measured faults, so we consider them representative only of local strain variations. With the exception of these reverse faults, none of the minor structures studied record the structural thickening that would be expected with reverse faulting or transpression across the fault zone.

The primary assumption we have made in further interpreting these fault groups in the following paragraphs is that structures that record similar strain are genetically related. Interestingly, minor faults from the Tijeras graben record shortening and extension directions similar to those from the Tijeras fault damage zone, despite differences in fault patterns and kinematics (Figs. 4, 5). East-northeast-striking right-lateral strike-slip and normal faults, north-northwest-striking left-lateral strike-slip faults, and northwesterly striking normal faults from the Tijeras greenstone and the Morrison, Abo, and Dakota formations all record south-southwest extension (Fig. 8A). Associated shortening directions trend generally east-southeast and exhibit a variety of plunges. The latter variation reflects the range in magnitude of the component of normal slip associated with movement on a given fault, where the plunge increases with an increase in the normal component of slip. Strike-slip faults record subhorizontal shortening. Note that although shortening directions are at a high angle to the fault they do not record reverse motion within the fault zone, because the extension recorded by these faults is subhorizontal, with the exception of the two reverse faults discussed previously.

Minor fault patterns from the damage zone of the Tijeras fault are dominated by east-northeast-striking, right-lateral strike-slip faults, which are strikingly similar to minor fault patterns from the damage zone of the Punchbowl fault (Fig. 3); the only significant difference is that they show less variation in strike and dip. Minor right-lateral strike-slip faults from the damage zone of the Tijeras fault generally dip more steeply than those of the Punchbowl fault, and the Tijeras fault also dips more steeply than the Punchbowl fault. These observations suggest that structures within the Tijeras damage zone record right-lateral strike-slip motion on the fault itself, rather than the right-lateral motion with a reverse component exhibited by the Punchbowl fault. Deformation in the damage zone of the Tijeras fault therefore appears to have been noncoaxial and to have been accomplished largely by Riedel shears (cf. Fig. 3C). As noted earlier, a number of these strike-slip faults also record a normal component of slip. We therefore interpret this largest group of faults as recording right-lateral and spatially variable north-side-down normal motion on the Tijeras fault. We suggest that the east-northeast-striking, dominantly right-lateral strike-slip faults are Riedel shears and the north-northwest-striking, left-lateral strike-slip faults are R′, or antithetic Riedel shears. Normal and oblique-normal faults record extension in this overall right-lateral transtensional regime. As indicated previously, east-northeast-striking faults bound lithologically distinct blocks within the tectonic mélange exposed near Golden; thus, these faults constitute an important part of the fault-zone structure.

East-northeast-striking normal faults near the southern margin of the Tijeras graben are in proximity and strike parallel to the major fault that bounds the Tijeras graben to the south, across which there is more than 1,200 m of vertical stratigraphic separation (Fig. 7). The spatial association and similar orientation of these faults suggest that they are genetically related. The pitch of slickenlines on northwest-striking dominantly normal faults in the same area varies from 60° to 80°. Slickenfibers and/or secondary fractures on three slickensides in the Abo Formation that contribute to this population record a dominant component of normal motion. These east-northeast- and northwest-striking faults collectively record similar extension and shortening directions to the population of faults described in the previous paragraph (Fig. 8). We therefore interpret the major fault that bounds the southwestern end of the Tijeras graben as a releasing bend between the Tijeras and Guiterrez faults during right-lateral transtension on the fault system.

The orientations of structures in the Cibola gneiss in Tijeras Canyon deserve further comment. As is evident in Figure 4, minor faults adjacent to the Tijeras fault are dominantly east-northeast-striking, and slickenlines record dominantly strike-slip displacement. Faults in the Cibola gneiss are a distinct exception to this pattern; they are dominantly east-northeast-striking faults with steeply pitching slickenlines. We do not know why faults in the Cibola gneiss are distinct in orientation and movement history. Perhaps transtensional movement was partitioned between the dip-slip faults in the Cibola gneiss and strike-slip faults in the adjacent Tijeras greenstone; perhaps most of the deformation occurred in the weaker greenstone.

Smaller subsets of the larger array of measured faults record very different shortening and extension directions.

Some of the faults measured in the Morrison and Abo formations, as well as the fault zone exposure near Golden, record northerly shortening and easterly subhorizontal extension (Fig. 8B). These faults include broadly north-striking dominantly normal faults, north-northeast- striking left-lateral strike-slip faults, and northwest-striking right-lateral faults. The latter two fault types are properly oriented for slip as R and R′ shears, respectively, during left-lateral strike-slip motion on the Tijeras– Cañoncito fault system (Fig. 8B). This left-lateral strike-slip movement may have been associated with normal motion as well; there is a significant variation in the plunge of shortening directions recorded by these faults.

Northeast-striking normal faults in the Abo and Morrison formations and a single northeast-striking, southeast-dipping, right-lateral normal fault in the Cibola gneiss record subvertical shortening and roughly northwesterly subhorizontal extension (Fig. 8C). The latter minor faults are interpreted as recording extension across the fault system.

In summary, minor faults provide a record of (a) transtension: dominantly right-lateral strike-slip with locally variable amounts of north-side-down normal motion, (b) left-lateral strike-slip, and (c) extension across the Tijeras–Cañoncito fault system. They do not provide any indication of the timing of these events. To evaluate timing, we consider additional geologic evidence and thermochronologic data.

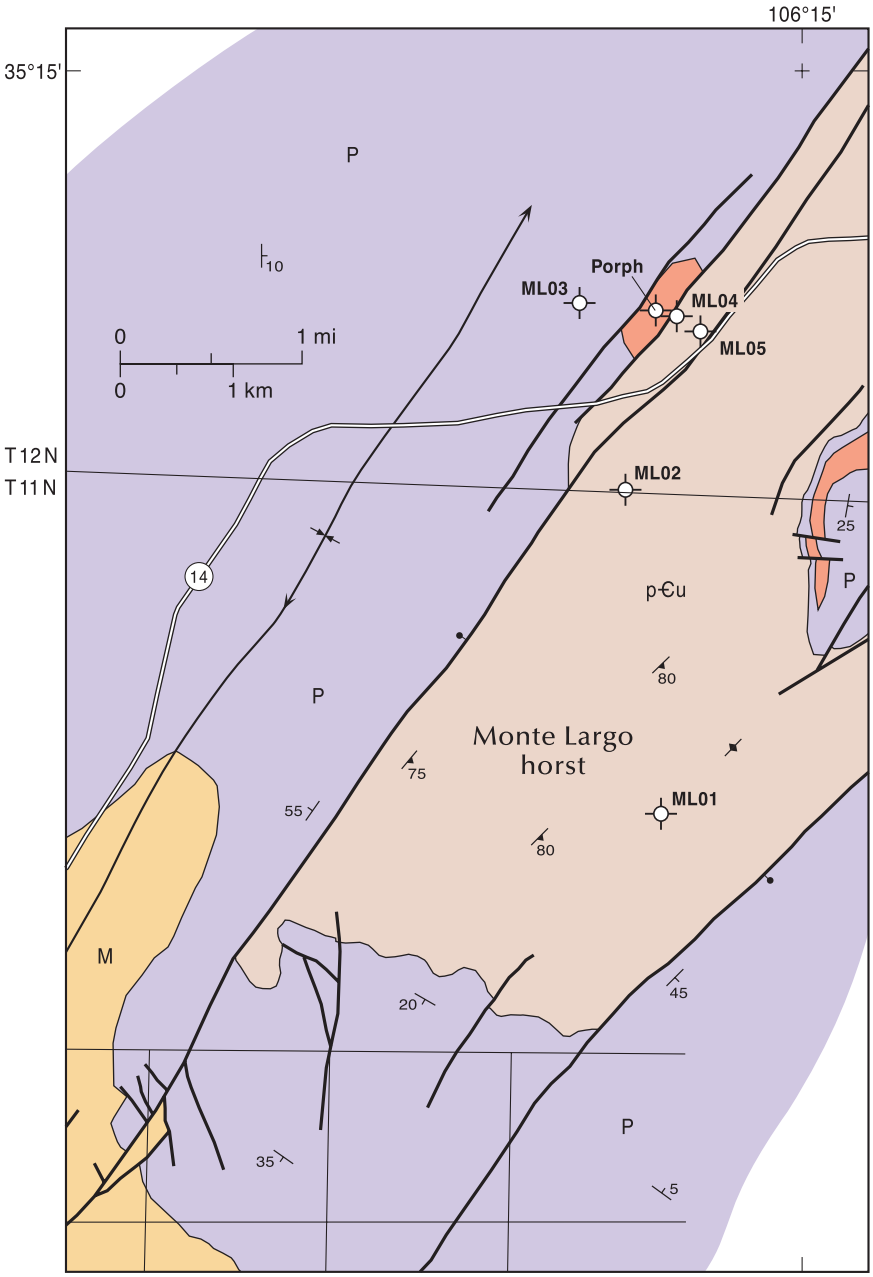

FIGURE 9—Sample localities for fission-track analysis in the Golden exposure. Map area is enlarged from upper right part of Figure 2, and uses the same symbols and patterns as Figure 2.

Evidence for the timing of movement on the Tijeras–Cañoncito fault system

Principles and methods of fission-track analysis

The principles behind fission-track analysis, a powerful tool for evaluating the differential cooling history across fault zones, are described in detail by Kelley and Chapin (2004 this volume, see especially their fig. 2). Fission-track analysis of apatite is routinely used in constraining the thermal history of rocks between ~ 60 °C and 110 °C. In zircon, fission tracks are stable to much higher temperatures: ~170–390 °C (Yamada et al. 1995). Fission-track analysis of rocks from both sides of a fault zone can constrain the timing of cooling due to differential uplift and erosion of the fault blocks and therefore the timing of substantial vertical displacement on the fault zone (Kelley and Chapin 2004 this volume). They do not constrain the timing or magnitude of strike-slip movement because the two fault blocks will not have significantly different thermal histories as a result of horizontal displacement.

Apatite and zircon fission-track (AFT and ZFT) ages were determined for several rocks proximal to the Tijeras fault zone (Figs. 2 , 9; Table 1) in an attempt to constrain the timing of vertical displacement. We chose a portion of the fault with significant stratigraphic separation for the analysis. The contact between Proterozoic basement and overlying Pennsylvanian strata exhibits 600–800 m of down-to-the-northwest separation across the Tijeras fault on the northwestern margin of the Monte Largo horst.

Samples were collected south of the village of Golden on a traverse across the Tijeras fault zone into the Monte Largo horst (Fig. 9). The units sampled on the traverse include Proterozoic Sandia granite and Cibola gneiss, Permian Abo siltstone, porphyritic intrusive rock of suspected Oligocene age (resembling porphyritic rocks exposed in the nearby Oligocene San Pedro–Ortiz porphyry belt), and a Quaternary deposit that was incorporated into the fault zone (Table 1). In addition, samples from the Cibola gneiss on the north side of I–40 (and the fault) and from the Tijeras

TABLE 1—Apatite and zircon fission-track data for Tijeras fault samples. ρ_s = spontaneous track density; ρ_i = induced track density (reported induced track density is twice the measured density; ρ_d = track density in muscovite detector covering Corning glass CN-5 (12.5 ppm U) and CN-6 (1.05 ppm U; reported value determined from interpolation of values for detectors covering standards at the top and bottom of the reactor packages (fluence gradient correction)); number in parenthesis is the number of tracks counted for ages and fluence calibration or the number of track measured for lengths). **s.e.** = standard error; **P(χ)²** = Chi-squared probability; **N.D**. = no data. $\lambda_f = 1.551 \times 10^{-10}yr^{-1}$, g = 0.5, zeta = 5,516 ± 300 for apatite, 452 ± 56 for zircon. Spectral peak ages calculated from Hurford et al. (1984); mean track lengths not corrected for length bias (Laslett et al., 1982).

Sample (elevation)	Lithology	Latitude Longitude	Phase	Number of grains dated	ρ_s x 10^5 t/cm²	ρ_i x 10^6 t/cm²	ρ_d x 10^4 t/cm²	Central age (Ma) (± 1 s.e)	Spectral peak ages Ma	P(χ)² %	Uranium content ppm	Mean track length µm (± 1 s.e.)	Standard deviation track length (µm)
94ML01 (2,134 m)	Sandia granite	35°11.41′ 106°15.51′	apatite	20	0.65 (48)	1.63 (604)	9.71 (4,100)	21.4 ± 3.3	19	99	17	N.D.	N.D.
94ML02 (2,027 m)	Sandia granite	35°13.21′ 106°16.11′	apatite	20	2.50 (145)	5.40 (1,566)	10.05 (4,100)	24.9 ± 2.4	22	97	58	13.5 ± 0.5 (65)	2.2
94ML03 (1,988 m)	Abo sandstone	35°13.69′ 106°15.77′	apatite	20	0.96 (26)	2.05 (278)	10.13 (4,100)	25.1 ± 5.2	21	95	22	N.D.	N.D.
			zircon	16	163.40 (1,349)	7.61 (314)	21.08 (4,334)	204.5 ± 17.3	188	15	451	N.D.	N.D.
PORPH (1,988 m)	Dacite porphyry	35°13.66′ 106°15.40′	apatite	20	0.79 (38)	1.95 (469)	11.96 (4,100)	26.4 ± 4.6	22	99	17	12.2 ± 2.1 (13)	3.8
			zircon	20	37.79 (820)	11.30 (1,226)	21.11 (4,334)	31.9 ± 2.0	31	90	678	N.D.	N.D.
94ML04 (1,988 m)	Cibola gneiss	35°13.63′ 106°15.69′	apatite	20	1.90 (129)	3.94 (1,340)	9.41 (4,100)	25.9 ± 2.6	22	94	42	13.2 ± 0.7 (21)	0.7
94ML05 (1,988 m)	Sante Fe sandstone	35°13.62′ 106° 15.66′	apatite	20	3.18 (145)	2.87 (655)	9.77 (4,100)	56.8 ± 8.4	22, 68	<1	31	N.D.	N.D
			zircon	25	48.85 (1,679)	8.75 (1,504)	21.14 (4,334)	50.0 ± 8.8	3, 27, 47, 95	<1	522	N.D.	N.D.
94TIJ02 (1,841 m)	Cibola gneiss	35°04.08′ 106°25.25′	apatite	20	1.75 (66)	4.96 (936)	11.91 (4,100)	23.0 ± 3.1	20	99	44	12.1 ± 1.9 (11)	3.3
95TC01	Tijeras greenstone	not available	apatite	35	0.09 (18)	0.27 (252)	10.40 (3,825)	20.1 ± 5.0	20	92	3	N.D.	N.D.

greenstone south of I–40 (and the fault; Fig. 2, Table 1) in Tijeras Canyon were analyzed.

The fission-track analysis methods used in this study are fully described in Kelley et al. (1992) and are briefly summarized here. Apatite and zircon were separated from the samples using standard heavy-liquid and magnetic separation techniques. Apatite grains were mounted in epoxy, polished to expose the grains, and etched for 25 seconds in a 5 M solution of nitric acid to reveal the fission tracks. Zircons were mounted in FEP Teflon tape, polished, and etched for 6 (samples ML03 and ML05) to 8 (PORPH) hrs in NaOH/KOH at 240 °C. Some of the zircon grains in the Quaternary deposit in the fault zone (ML05) were underetched after 6 hrs. Consequently, a second mount of the sample was prepared and etched for 9 hrs to reveal tracks in the youngest grains; the individual detrital zircon grain ages include analysis of both the 6 hr and 9 hr mounts. Tracks parallel to the c-axes of the dated zircons were well etched in all mounts. Zircons from the Proterozoic rocks were etched for 1 hr and found to be metamict. The grain mounts were then covered with muscovite detectors and sent to the Texas A&M Nuclear Science Center for irradiation. The neutron flux was calibrated with Durango apatite and Fish Canyon zircon age standards and Corning Glasses CN-5 and CN-6 using the zeta method (Hurford and Green 1983). A zeta value of 5,516 ± 300 was determined using the CN-6 glass and the accepted age of 31.4 ± 0.5 for Durango apatite (Green 1985). A zeta value of 452 ± 56 was determined using CN-5 glass and the accepted age of 27.8 ± 0.7 Ma for Fish Canyon zircon. Individual grain ages were calculated using the methods of Hurford and Green (1983), and the Chi-squared statistic (Galbraith 1981) was applied to determine whether the individual ages belong to a single population. Mixed ages caused by differences in sedimentary provenance for zircon and apatite or by partial annealing of apatite with variable chemical composition are indicated when the ages do not pass the Chi-squared statistic at the 5% probability level. If the individual-grain ages passed the Chi-squared test, the pooled age was computed using the methods of Galbraith and Laslett (1985). If the sample failed the Chi-squared test, the central age, a weighted mean age estimate that eliminates a bias toward grains with higher mean track densities, was calculated as outlined by Galbraith and Laslett (1993). The pooled age and central age are identical for Chi-squared probabilities > 85%.

Two graphical techniques are often employed to evaluate the ages and relative importance of multiple dated grain populations. The first involves calculating the probability density function for the grains (Hurford et al. 1984). The probability distributions for all the grains are summed to give a weighted spectrum of the population. The age spectrum, which is usually scaled to and superimposed on the grain age histogram, indicates the probability that a certain number of grains in a sample will have ages within a given age interval. Peaks on the age spectrum are referred to as 'spectral peak' ages (Table 1). Multiple grain age populations can also be analyzed using radial plot diagrams (Galbraith 1988), which allow comparison of measurements with different standard errors. The variation of the single grain ages around the mean are plotted as $y = (z_i - z)/s.e._i$, where z_i is the individual grain age, z is the mean age, and $s.e._i$ is the standard error of the single grain age, versus $x = 1/s.e.$; a measure of the precision of each grain age. The fission-track age is given by the slope of a straight line from the origin through the data points. The age scale is shown radially around the edge of the plot. Because young grains have precise grain ages, these grains are easily identified because they plot to the right on the diagram. If the grains all belong to a single age population, the points should lie within $y = \pm 2$, which corresponds to lying within ± 2 s.e. Scatter outside $y = \pm 2$ indicates that multiple populations are present. The ages and relative mixing proportions of the populations can be estimated from clustering of the data on the diagram.

Confined track-length distributions in the apatite-grain mounts that were etched with the age mounts were deter-

mined using a microscope fitted with a 100X dry lens, a drawing tube, and a digitizing tablet. Horizontal, well etched, confined tracks (tracks completely enclosed within the crystal) in grains with prismatic faces were measured. The orientations of the tracks with respect to the c-axis were also determined.

Time-temperature estimates were derived from the apatite age and track-length data using the model of Ketchum et al. (1999). This inversion model is used to determine time-temperature paths that fit the observed age and length data. The model accounts for the influence of variable apatite composition on track annealing. The tendency to measure long tracks rather than short tracks due to observational bias is corrected using the methods of Laslett et al. (1982).

Fission track results

The AFT ages of the bedrock units on both sides of the Tijeras fault zone in the vicinity of Golden and in Tijeras Canyon are similar (Table 1). Samples of Sandia granite within (ML01) and near the northeastern margin (ML02) of the Monte Largo horst, porphyritic intrusive rock (PORPH) and Cibola gneiss (ML04) within the fault zone, and Abo siltstone on the northwest fault block (ML03), all from the transect near Golden, as well as Cibola gneiss (TIJ2) and Tijeras greenstone (TC1) from Tijeras Canyon, have AFT ages between 21.4 ± 3.3 and 26.4 ± 4.6 Ma (late Oligocene to early Miocene; Table 1; Fig. 10). The mean track lengths for samples containing more than 20 confined tracks are 13.2–13.5 μm. These results are comparable to previously published AFT data for the Sandia Mountains (Kelley and Duncan 1984, 1986; Kelley et al. 1992) and suggest regional denudation in the early Miocene (Kelley and Chapin 1995).

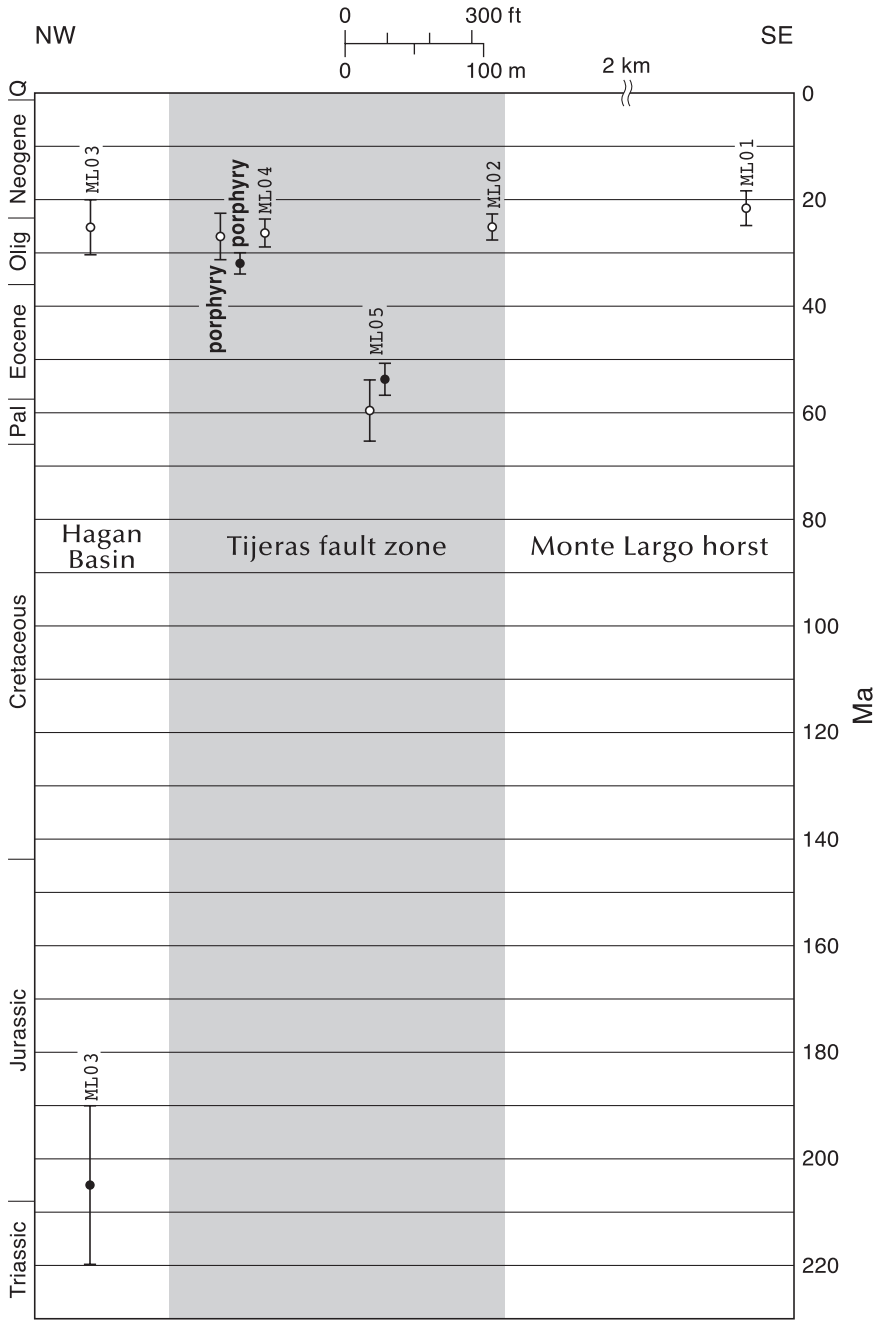

FIGURE 10—Comparison of fission-track ages in and adjacent to the Tijeras fault near Golden. Error bars represent 1 standard error. Open circles represent AFT ages; solid circles represent ZFT ages.

In contrast, zircon fission-track (ZFT) dates on the samples vary widely (Table 1). The ZFT age of the porphyritic intrusive rock is 31.9 ± 2.0 Ma. The rock has a porphyritic texture defined by 1-5 mm phenocrysts of altered hornblende and plagioclase in an aphanitic matrix. Alteration is sufficiently extensive that $^{40}Ar/^{39}Ar$ dating is not possible. The porphyritic texture and aphanitic matrix suggest rapid cooling and crystallization, probably related to emplacement at shallow crustal levels. The ZFT age records the time since cooling below the closure temperature of zircon; because cooling is expected to occur rapidly following shallow intrusion, the ZFT age is taken as an approximate emplacement and crystallization age. The ZFT age is younger than hornblende $^{40}Ar/^{39}Ar$ ages of 34.5 ± 0.2 Ma and 35.02 ± 0.13 Ma obtained on a porphyry dike and a plug, respectively, located ~ 4 km west-northwest of this exposure (Ferguson et al. 1999). The relationship between these intrusive bodies and the one we have studied is not clear. The ZFT date on the porphyritic intrusive rock in the Golden exposure falls within the range of $^{40}Ar/^{39}Ar$ ages exhibited by porphyritic intrusive rocks of the Ortiz Mountains, documented in the following section, that outcrop along the Tijeras fault to the northeast. These ages are similarly interpreted as approximate emplacement ages and are consistent with our interpretation of the ZFT date as an approximate emplacement age. The porphyritic intrusive rock is intensely fractured and contains anastomosing gouge-lined faults (Abbott and Goodwin 1995); therefore some deformation within the Tijeras fault zone post-dates intrusion (32 ± 2 Ma) at this site. The intrusive rock is locally faulted against Quaternary surficial deposits; however, this fault is overlain by younger, undeformed and imbricated Quaternary gravel deposits (Abbott and Goodwin 1995).

AFT ages of rocks adjacent to the porphyritic intrusive

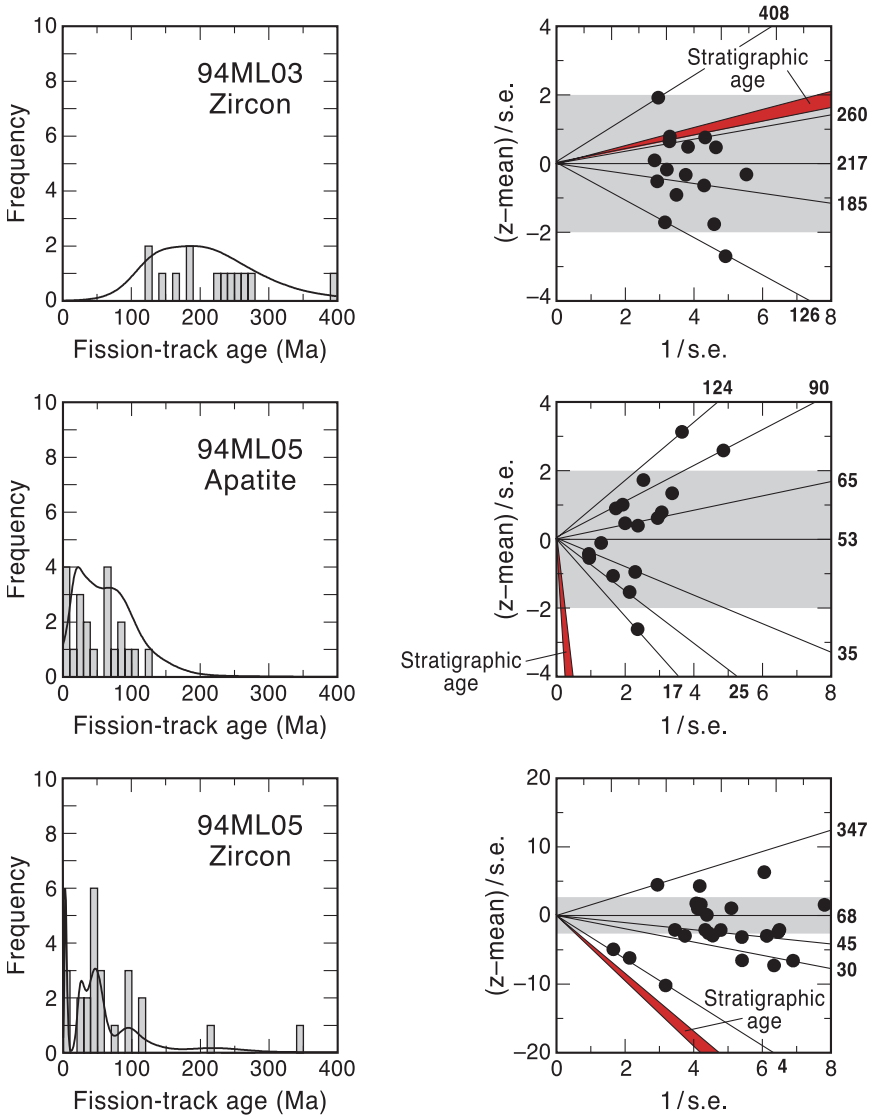

FIGURE 11—Apatite and zircon fission-track age histograms and probability density functions (solid curves) for Abo siltstone (94ML03) and deformed Quaternary surficial deposit (94ML05) shown on the left side of the diagram. Peak ages in Table 1. Radial plots for the same samples shown on the right side of the diagram. Radial plots are defined in the text; **z** = mean age (coincides with y = 0) and **s.e.** = standard error. The fission-track ages are shown around the edges of the radial plots. The gray region corresponds to the 2 σ error in the mean age and the red area shows the stratigraphic ages of the sedimentary rocks.

rock are similar to AFT ages of the intrusion and samples in Tijeras Canyon approximately 20 km away (Table 1; Fig. 2), and are comparable (within error) to the AFT ages from the northwest side of the Sandia Mountains (16 to 22 Ma) and the Pedernal Hills to the east (22–33 Ma; Kelley and Duncan 1984, 1986; Kelley and Chapin 1995). The similarity of AFT ages over most of the High Plains of northeastern New Mexico indicates that the AFT ages record regional cooling. The porphyritic intrusive rock therefore was emplaced before the time of regional cooling below the closure temperature of apatite.

The individual grain ages of zircons from the Permian Abo siltstone west of the Tijeras fault zone fail the Chi-squared test, indicating multiple age populations within this siltstone. Consequently, a central age, which is a weighted mean age, is reported for this sample (Table 1). The central fission-track age for the zircon in the Permian Abo siltstone, however, is Middle Triassic–Middle Jurassic: 205 ± 30 Ma (2 s.e.). Clearly, this date does not reflect the age(s) of the source rocks, as it is younger than the depositional age of the siltstone. As more than half of the individual grain ages are younger than the stratigraphic age (Fig. 11), the apparent ZFT ages record partial annealing (temperatures > 170 °C; Hurford 1986) after Permian time.

AFT and ZFT ages were determined for detrital grains from Quaternary(?) sand (ML05) incorporated into the eastern margin of the Tijeras fault zone in order to establish the provenance of the deposit. The ZFT ages will constrain the maximum age of this unit, especially if some of the detrital zircon came from Pliocene to Quaternary volcanic centers in the Jemez Mountains. The individual grain ages for both apatite and zircon from the Quaternary deposit fail the Chi-squared test and central ages are reported for this sample (Table 1). The deformed Quaternary deposit contains grains that have ZFT ages ranging from late Paleozoic to Pliocene (Fig. 11). A large fraction of the dated grains are Paleogene in age and some probably were incorporated from the porphyritic intrusive rock, which is in fault contact with the deposit. Three grains with ZFT ages between 3.2 ± 1.0 and 4.3 ± 2.0 Ma were likely derived from a Pliocene volcanic source to the northwest (e.g., Bachman and Mehnert 1978). AFT dates on individual grains in the sample are also highly variable, ranging from 17.5 ± 7.4 to 124.0 ± 34.0 Ma (Fig. 11). Several grains in the deformed surficial deposit have AFT dates that are Mesozoic in age. These Mesozoic AFT ages (clustering around 68 Ma; Fig. 11; Table 1) are dissimilar to the AFT ages in Proterozoic bedrock samples from both this area and the Sandia Mountains to the west (from 21.7 ± 2.3 to 16.3 ± 1.8 Ma; House et al. 2003). Most of the grains with Mesozoic AFT ages in the deformed Quaternary deposit are round to subround and thus presumably were derived from Mesozoic sedimentary rocks exposed on the west side of the Sandia Mountains. These Mesozoic ages may reflect the cooling of the sedimentary section above Proterozoic basement during Laramide deformation, subsequent to burial during Cretaceous time. Sampling of Mesozoic sedimentary rocks west of the Sandia Mountains is needed to evaluate this hypothesis. The ages of the youngest dated apatite (17 Ma) and zircon (3–4 Ma) populations are older than the inferred stratigraphic age of the surficial deposit (Fig. 11), so temperatures in the fault zone in the Quaternary were not high enough to totally reset the fission-track ages. The youngest ZFT ages indicate that the maximum age of the deposit is Pliocene.

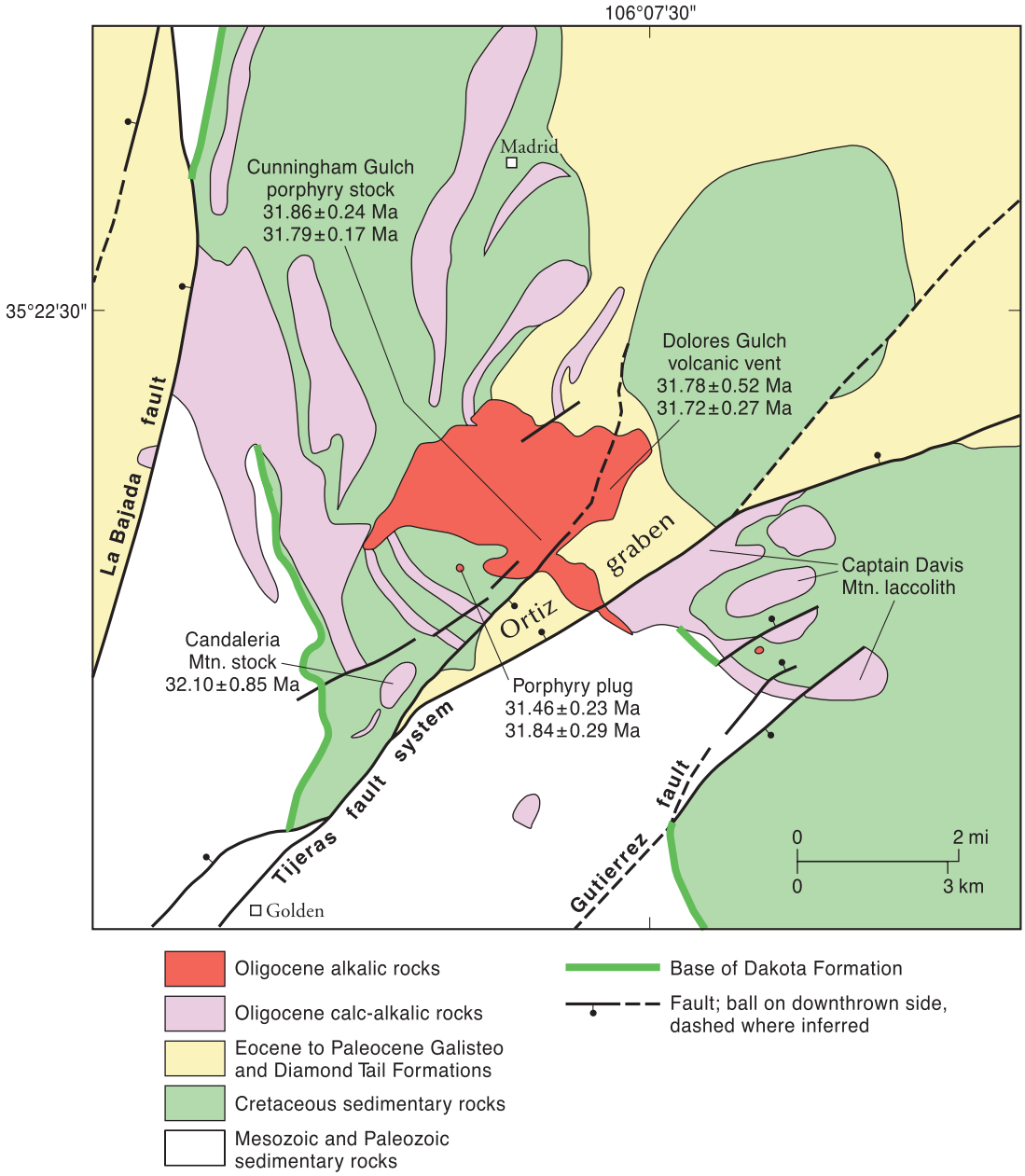

FIGURE 12—Simplified geologic map of the Ortiz Mine Grant, modified from Maynard (1995). Sites from which $^{40}Ar/^{39}Ar$ samples were collected are shown.

$^{40}Ar/^{39}Ar$ analysis of igneous rocks from the Ortiz Mountains

Geologic context

The geology of the Ortiz Mountains, northeast of the village of Golden, New Mexico (Figs. 1, 12), has been described by Maynard et al. (1990) and Maynard (1995). A brief summary of key points is included below as context for the $^{40}Ar/^{39}Ar$ ages we report below.

The relationships between Oligocene intrusive bodies, sedimentary rocks of Permian through Eocene age, and the Tijeras–Cañoncito fault system provide important information about the relative timing of deformation and intrusion in the Ortiz Mountains. The sedimentary rocks exhibit 10–30° eastward dips, believed to have developed during Miocene opening of the Rio Grande rift. The principal structure in this area is the Ortiz graben, which formed subsequent to deposition of the Paleocene Diamond Tail and Eocene Galisteo formations. The base of the Diamond Tail Formation exhibits normal stratigraphic separations of 610 and 1,220 m on the graben's northwestern and southeastern bounding faults, respectively. The rhomb shape of the Ortiz graben and orientations of bounding faults have been interpreted to record extension during dominantly left-lateral strike-slip movement on the fault system (Maynard 1995; Fig. 12).

The Ortiz Mountains include rocks of the Ortiz porphyry belt, a collection of Oligocene stocks, laccoliths, sills, and dikes that intrude Pennsylvanian through Tertiary sedimentary rocks. The intrusive rocks can be divided into older calc-alkaline laccoliths and younger alkaline stocks. The oldest calc-alkaline intrusives—andesite porphyry laccoliths, sills, and dikes—were emplaced into rocks at all stratigraphic levels across the Ortiz graben. K-Ar dates on the older calc-alkaline laccoliths suggest that they were intruded ca. 34 Ma (Bachman and Mehnert 1978; Kay 1986; Sauer

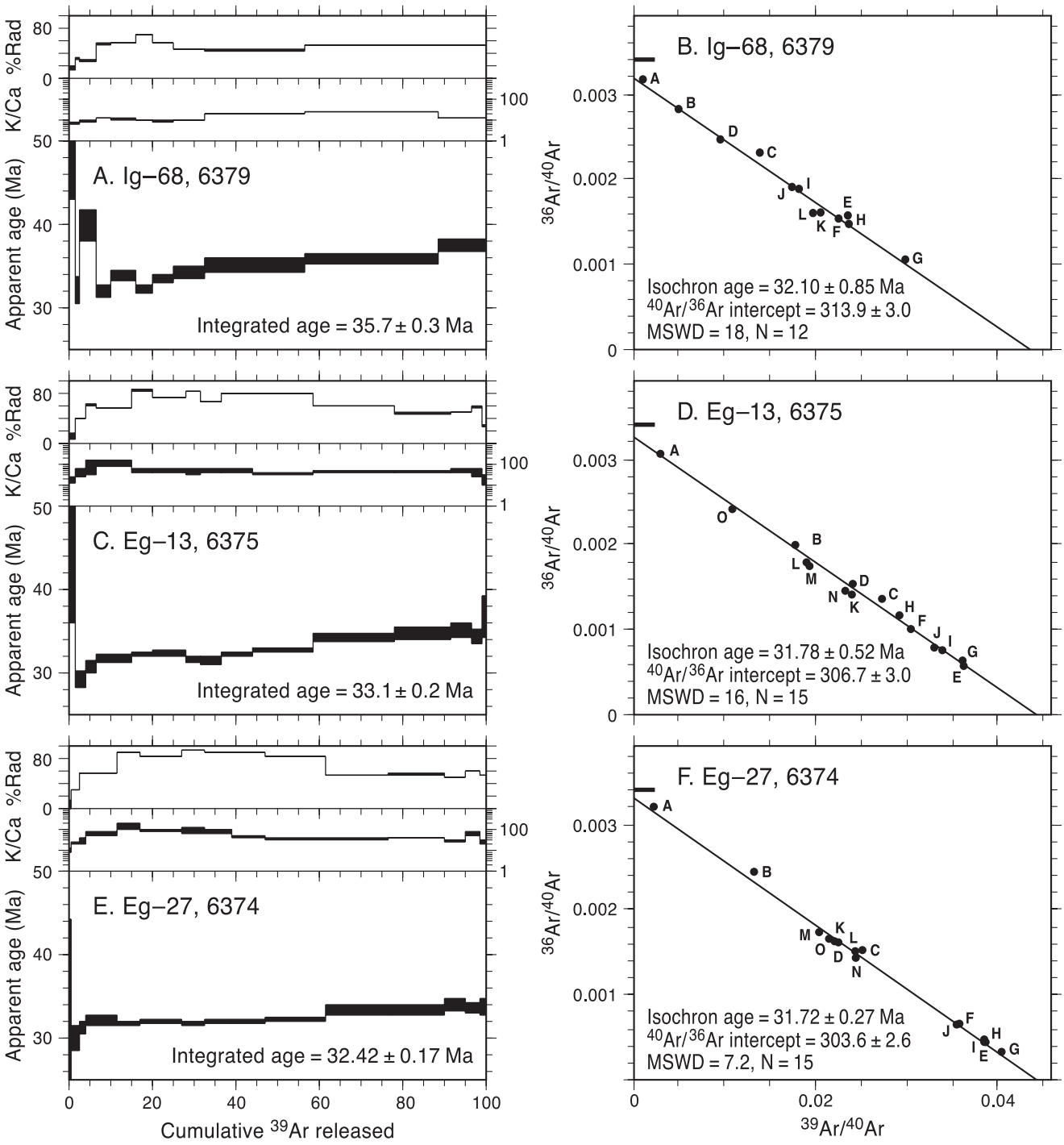

FIGURE 13—Results of $^{40}Ar/^{39}Ar$ dating of K-feldspar separates from the Ortiz Mine Grant. (**A–J**) Age spectra and inverse isochron diagrams for incrementally heated samples. All of the $^{40}Ar/^{36}Ar$ isochrons intercepts are significantly elevated relative to atmospheric argon ($^{40}Ar/^{36}Ar = 295.5$) indicating homogeneous trapped excess ^{40}Ar components. The circles depicting data points are larger than the actual error elipses. (**K–L**) Age-probability distribution diagrams (Deino and Potts 1992) for samples analyzed by single-crystal laser-fusion.

1999). Most of these bodies are concordant with bedding and are locally cut by strands of the Tijeras–Cañoncito fault system, exhibiting left-lateral separation, like the sedimentary rocks they intrude. The distribution of sills in the Cretaceous section on the Ortiz Mine Grant shows one laccolithic center in the western part of the Ortiz Mountains north of the Tijeras fault and another at Captain Davis Mountain south of the Tijeras fault. A similar magnitude of left-lateral separation, roughly 5 km, is exhibited by the base of the ~ 30° east-tilted Cretaceous Dakota Formation. However, if the Miocene rotation mentioned above is removed, this separation can be interpreted to record northwest-side-down normal displacement, which could have been accompanied by left-lateral strike-slip movement.

The younger suite of intrusive rocks cut both the older intrusive bodies and the fault. Only the oldest units of the younger alkaline suite exhibit displacement, and the magnitude of separation is much less than that exhibited by the older calc-alkaline intrusive rocks. Thus the timing of the most recent movement on this portion of the fault system is

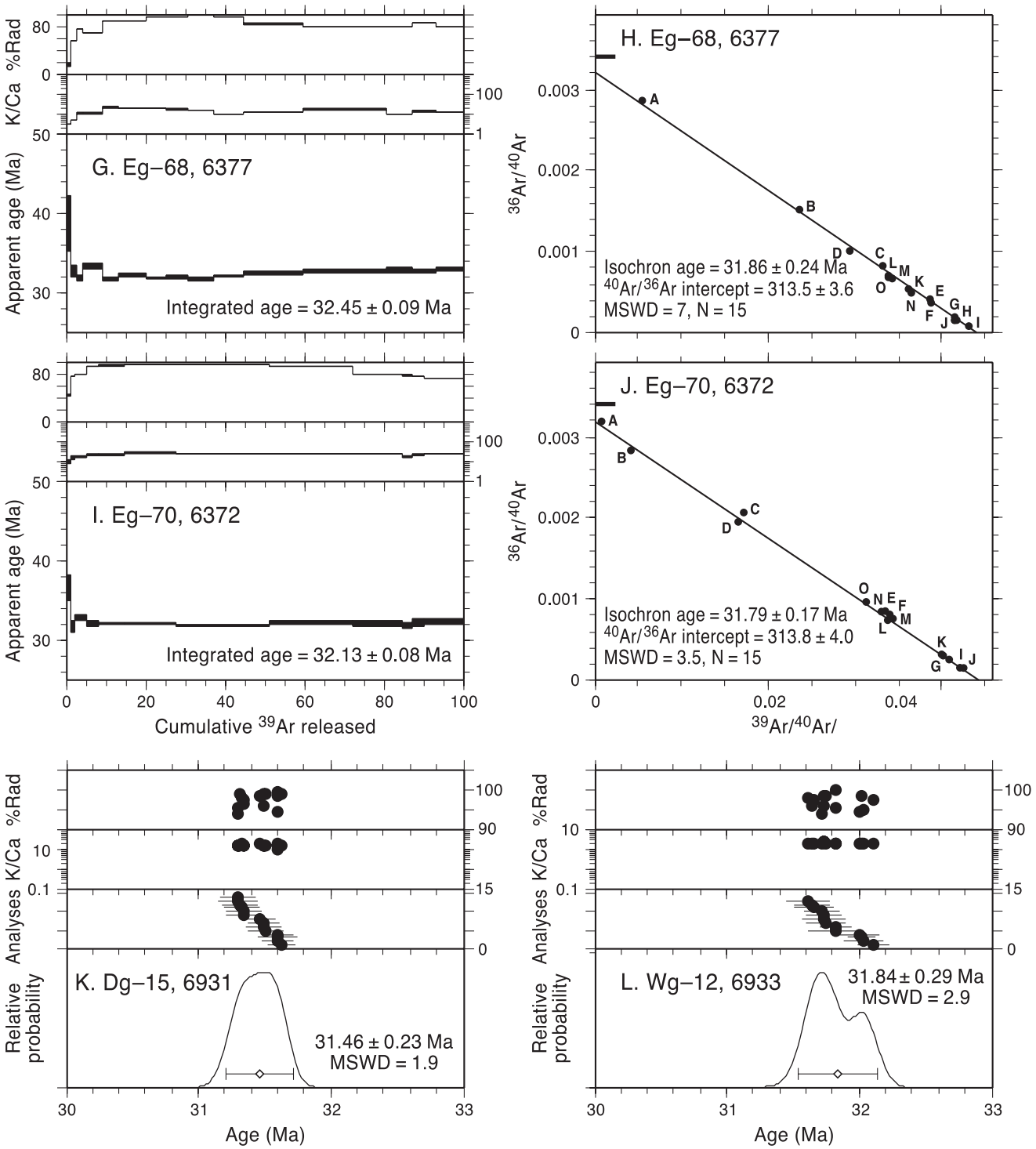

FIGURE 13 continued.

constrained by the ages of the youngest igneous rocks in the Ortiz Mountains.

$^{40}Ar/^{39}Ar$ methods and results

To provide a minimum age of formation of the Ortiz graben and northwest-side-down normal displacement (and possible left-lateral strike-slip motion) of the older rocks of the Ortiz porphyry belt, we obtained $^{40}Ar/^{39}Ar$ dates on K-feldspars from a variety of igneous rocks in the Ortiz Mountains. K-feldspar separates from seven of intrusive and extrusive igneous rocks within the Ortiz porphyry belt were prepared and analyzed at the New Mexico Geochronology Research Laboratory in Socorro, New Mexico. K-feldspar separates were prepared by standard separation techniques, then were irradiated at the Texas A&M reactor in two irradiation packages. Neutron flux was monitored using Fish Canyon Tuff sanidine (27.84 Ma; Deino and Potts 1990, equivalent to Mmhb-1 at 520.4 Ma, Samson and Alexander 1987). Samples were analyzed at the New Mexico Geochronology Research Laboratory. Monitor

TABLE 2—$^{40}Ar/^{39}Ar$ dating results from Ortiz K-feldspars. **UTM** coordinates relative to NAD 27, Analysis is incremental heating inverse isochron age or single-crystal laser-fuion (SCLF) weighted mean age; **n** is number of steps or fused crystals, **$^{40}Ar/^{36}Ar$** is trapped component ± 2σ, **MSWD** is mean sum of weighted deviates.

Lithology and geologic setting	Sample	UTM coordinates E	N	Analysis	n	K/Ca	$^{40}Ar/^{36}Ar$	MSWD	Age (Ma)±2σ
Tgd Candelaria Mtn. granodiorite stock. Assoc. with Cu-Au skarn mineralization at Lukas Canyon	Ig-68	392894	3907258	Isochron	12	15.7	313.9 ± 3.0	18.0	32.10 ± 0.85
Tv Lithic tuff, Dolores Gulch Espinaso volcanics	Eg-13	396403	3910803	Isochron	15	45.8	306.7 ± 3.0	16.0	31.78 ± 0.52
	Eg-27	396391	3910494	Isochron	15	49.5	303.6 ± 2.6	7.2	31.72 ± 0.27
Tl porphyry plugs	Dg-15	393379	3909455	SCLF	14	16.5	–	1.9	31.46 ± 0.23
	Wg-12	393379	3909455	SCLF	13	20.8	–	2.9	31.84 ± 0.29
Tl Feldspar porphyry	Eg-68	395294	3910176	Isochron	15	13.4	313.5 ± 3.6	7.0	31.86 ± 0.24
Subvolcanic instrusion, forms core to Cu-Au porphyry mineralization, upper Cunningham Gulch	Eg-70	395512	3910303	Isochron	15	15.7	313.8 ± 4.0	3.5	31.79 ± 0.17
Mean Ortiz age					7				31.74 ± 0.19

Methods:
Sample preparation: crushing, heavy liquid, Franz, HF etching, ultrasonic cleaning.
Irradiation: two separate in vacuo 7 hr irradiations (NM-47, NM-54), D-3 position, Nuclear Science Center, College Station, TX.
Neutron flux monitor: sample FC-1 of interlaboratory standard Fish Canyon Tuff sanidine with an assigned age of 27.84 Ma (Deino and Potts 1990), equivalent to Mmhb-1 at 520.4 Ma (Samson and Alexander 1987). Samples and monitors irradiated in alternating holes in machined Al discs.
Laboratory:
New Mexico Geochronology Research Laboratory, New Mexico Institute of Mining and Technology, Socorro, NM.
Instrumentation: Mass Analyzer Products 215-50 mass spectrometer on line with automated, all-metal extraction system.
Heating: single-crystal laser-fusion (SCLF): 10W continuous CO_2 laser; other samples: 5–8 mg aliquots in resistance furnace.
Reactive gas cleanup: SAES GP-50 getters operated at 20°C and ~ 450 °C.
Age and error calculations: all errors reported at ±2 σ. SCLF mean ages and errors calculated using inverse variance weighting of Taylor (1982) with errors multiplied by square root of MSWD where MSWD > 1.0 . Inverse isochron calculations after York (1969), with errors multiplied by square root of MSWD where MSWD > 1.0. Decay constant and isotopic abundances: Steiger and Jäeger (1977). Complete data set: Appendices 1 and 2, this volume.
Analytical parameters:
electron multiplier sensitivity = 1.7×10^{-17} moles/pA; typical system blanks were 87, 3 , 1 , 2, 3×10^{-18} moles (laser) and at 898, 6 , 1 , 1, $4 \times 10 \pm -18$ moles (furnace) at masses 40, 39, 38, 37, 36 respectively; . J-factors determined to a precision of ± 0.2% using SCLF of 4–6 crystals from each of 4–6 radial positions around irradiation vessel. Correction factors for interfering nuclear reactions, determined using K-glass and CaF_2, $^{40}Ar/^{39}Ar_K = 0.00020 \pm 0.0003$; $^{36}Ar/^{37}Ar_{Ca} = 0.00026 \pm 0.00002$; and $^{39}Ar/^{37}Ar_{Ca} = 0.00070 \pm 0.00005$.

sanidines and clear, sanidine-like K-feldspars from two rhyolite dikes were analyzed by single-crystal laser fusion, and K-feldspar separates from the remaining five samples were analyzed by resistance-furnace incremental heating. The composition and structural state of the dated K-feldspars were not quantitatively characterized. Details of sample preparation, irradiation, and analytical procedures are described in the footnotes to Table 2. Results are summarized in Table 2 and Figures 13 and 14, and complete analytical data are listed in Appendices 1 and 2. In addition to K-feldspars, we also attempted and failed to date hornblende separates from five samples. These analyses, which are not reported here, yielded irregular spectra and poorly correlated arrays on isochron plots.

Age spectra from the five incrementally heated K-feldspar separates are slightly to significantly discordant (Fig. 13A,C,E,G,I); none define flat age plateaus that meet plateau criteria (such as those of Fleck et al. 1977). However, when plotted on inverse isochron diagrams (Fig. 13B,D,F,H,J), data from all five K-feldspar separates form relatively well defined linear arrays (MSWD = 3.5 to 18), with $^{40}Ar/^{36}Ar$ intercepts ranging from 303.6 ± 2.6 to 313.9 ± 3.0. These $^{40}Ar/^{36}Ar$ intercepts significantly exceed the atmospheric value of 295.5, indicating that these samples contain small but significant trapped components of homogeneously distributed excess ^{40}Ar. Accordingly, the isochron intercept ages (Table 2) are considered to be the best estimate of the emplacement ages of these units.

Laser-fusion analyses of the clear, sanidine-like K-feldspars from the two rhyolite dike samples yielded tight, unimodal clusters of precise single-crystal ages (Fig. 13J,K) from which weighted-mean ages were calculated. Because of their high radiogenic yields (generally > 95%), isochron analysis was not effective for assessing the presence or absence of excess ^{40}Ar. However, as a second consequence of the high radiogenic yields, quantities of excess ^{40}Ar similar to those detected in the incrementally heated samples would have little effect on the calculated weighted-mean ages of these two samples. Hence, these weighted mean ages are considered to be accurate estimates of emplacement ages of these two dikes.

The isochron and weighted-mean ages of the seven dated samples all overlap within 2 σ, ranging from 32.10 ± 0.85 Ma to 31.46 ± 0.23 Ma (Fig. 14). The weighted mean of the seven $^{40}Ar/^{39}Ar$ ages is 31.74 ± 0.19 Ma. We conclude that all of the dated samples from the Ortiz Mine Land Grant cooled through their closure temperatures over a short interval near 31.75 Ma. Because K-feldspars have closure temperatures with respect to argon diffusion of ~ 150–300 °C, and because the dated intrusions are demonstrably shallow, the feldspar dates should closely approximate emplacement ages. The analytical uncertainties at the ± 2σ level permit a maximum emplacement interval for all seven dated samples as long as 1.7 m.y., although the actual duration of Ortiz igneous activity may have been much shorter.

$^{40}Ar/^{39}Ar$ constraints on timing of faulting

We were only able to date one rock from the older calc-alkaline suite—the Candelaria Mountain granodiorite stock (Tgd, Ig-68; Table 2; Fig. 14), which unfortunately does not interact with the fault system. The isochron age of 32.10 ±

0.85 Ma is the oldest date obtained, but the large uncertainty makes it indistinguishable from the ages of the younger rocks.

The Golden fault strand of the fault system terminates in the lithic tuff of Dolores Gulch (Tv, isochron ages of 31.78 ± 0.52 Ma and 31.72 ± 0.27 Ma, Table 2; Fig. 14) and a variety of feldspar porphyry bodies (Tl, single-crystal laser-fusion ages of 31.46 ± 0.23 Ma and 31.84 ± 0.29 Ma and isochron ages of 31.86 ± 0.24 Ma and 31.79 ± 0.17 Ma, Table 2; Fig. 14).

Collectively, these data indicate that: 1) the fault in this area was essentially in its present configuration by ca. 32 Ma; 2) northwest-side-down normal motion and possible associated left-lateral movement occurred in the Oligocene on this section of the fault (postdating deposition and lithification of the Eocene Galisteo Formation, and predating the final stages of ca. 32 Ma intrusion and volcanism); and 3) there has been no movement of significance on the fault system northeast of Golden subsequent to ca. 32 Ma. The latter conclusion is consistent with previous assertions that Quaternary movement on the Tijeras-Cañoncito fault system was restricted to the southwestern portion of the fault system (Machette et al. 1998).

Additional timing constraints

As mentioned earlier previous workers have considered whether or not the Tijeras fault was active in Precambrian time (e.g., Lisenbee et al. 1979; Connolly 1982). To address this issue, we have evaluated two possibilities: 1) the fault is a reactivated Precambrian ductile shear zone, and 2) the fault initiated in the Precambrian as a brittle structure. To consider the first of these options, we note the marked discordance between the orientation of the Tijeras fault and the orientations of the main Precambrian foliations on either side of the fault (Fig. 2). The foliation in the Tijeras greenstone strikes subparallel to locally oblique to the Tijeras fault, but dips moderately to the southeast. The foliation in the gneiss also strikes subparallel to the fault, but it dips moderately to the northwest. We have observed no significant strain gradient in the Cibola gneiss, and there is an absence of intensely sheared rocks in outcrop or as breccia clasts along the trace of the fault. The absence of both a fault-parallel foliation and an increase in strain magnitude with proximity to the fault argue against a ductile precursor to the Tijeras fault.

Lisenbee et al. (1979) and Connolly (1982) suggested that an apparent en echelon pattern of dikes and veins in the Tijeras greenstone indicated that sinistral strike-slip faulting was synchronous with intrusion of the Sandia granite. We have observed, however, that these pegmatite and aplite dikes and veins invariably lie within the plane of the foliation, so their orientation in three dimensions is controlled at least in part by the existing mechanical anisotropy and is not consistent with sinistral shear. The dikes and veins appear to be en echelon only because they are intruded along the foliation in the Tijeras greenstone, which is itself oblique to the Tijeras fault. In addition, minor fault patterns in Precambrian rocks are identical to those in younger rocks (Figs. 4, 5), indicating that the Precambrian units do not preserve evidence of brittle deformation that predated deposition of the younger rocks in the area.

Lisenbee et al. (1979) believed the differences in the Pennsylvanian Sandia Formation across the fault were due to syndepositional Pennsylvanian motion on the Tijeras fault, with the northwest side down. Our work indicates that on the southeast side of the Tijeras fault, the Pennsylvanian Sandia Formation is composed of roughly equal proportions of conglomerate, sandstone, and mudstone. The base of the formation is a matrix-supported sandy conglomerate about 1 m thick with rounded quartzite clasts up to 8 cm in diameter. On the northwest side of the fault, the basal conglomerate is 1–25 m thick, and the formation is dominated by sand and conglomerate, with lesser amounts of mudstone. Clasts in the conglomerate on the northwest fault block are generally similar in size to those on the southeast fault block, although locally there are boulders up to 1 m in diameter immediately adjacent to a ridge of Proterozoic quartzite that evidently was a topographic high in Pennsylvanian time. An alternative explanation for these observations is that different facies were juxtaposed subsequent to deposition by strike-slip motion on the fault. This interpretation is further supported by the fact that the Sandia Formation on the northwest fault block is highly variable in lithology and thickness, demonstrating laterally abrupt facies changes within the formation.

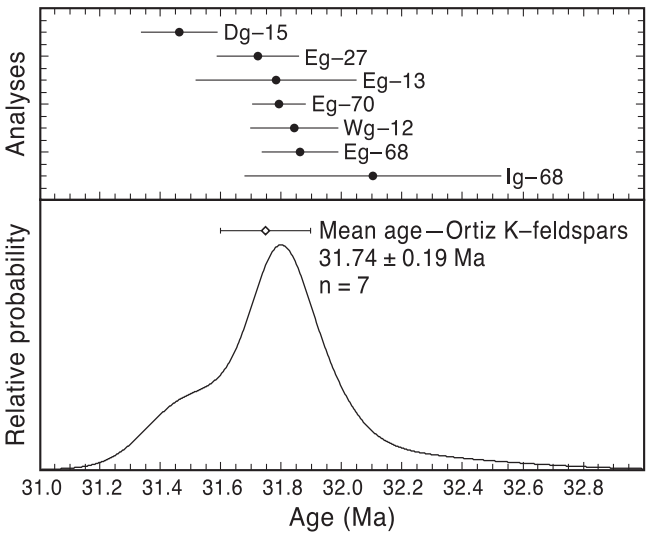

FIGURE 14—Age-probability distribution diagram summarizing $^{40}Ar/^{36}Ar$ ages of K-feldspar separates from the Ortiz Mine Grant. All seven age determinations overlap at 2 σ; the weighted mean age is 31.74 ± 0.19 Ma.

Discussion and conclusions

Timing of deformation events

To evaluate timing, we begin with evidence for the youngest motion on the fault system, and work toward an evaluation of the oldest deformation. Quaternary movement on the Tijeras fault has been documented by a number of previous workers (Lisenbee et al. 1979; Abbott and Goodwin 1995; Lisenbee and Woodward 1995; Machette et al. 1998; Kelson et al. 1999). Machette et al. (1998) noted an absence of evidence for Quaternary motion northeast of Golden. This is consistent with our $^{40}Ar/^{39}Ar$ data, which indicate that slip on the Tijeras-Cañoncito fault system in this area ceased by ca. 32 Ma, the age of igneous rocks that truncate strands of the fault system. In contrast fission track data indicate that a highly brecciated porphyritic intrusive rock at the Golden site is similar in age to rocks of the Ortiz belt, ca. 32 Ma. This leads us to speculate that Quaternary motion on the Tijeras fault has largely accommodated extension on the La Bajada fault by movement of the southwestern segment of the Tijeras fault, a possibility first suggested by Kelley and Northrop (1975).

Kelson et al. (1999) presented geomorphic evidence that Quaternary motion on the Tijeras fault was left-lateral strike-slip. These data are consistent with the Tijeras fault acting as a transfer fault to accommodate extension on the La Bajada fault. Ferguson (1999) suggested that the Tijeras

fault actually initiated in the Miocene as a transfer fault and has only been active as a left-lateral strike-slip fault. He suggested that folds that previous workers interpreted as recording right-lateral strike-slip motion were developed during movement on the Gutierrez fault. We do not agree with this interpretation for three reasons. First, fission track data indicate that uplift of the Monte Largo horst across the Tijeras fault was accomplished before the late Oligocene. Second, the $^{40}Ar/^{39}Ar$ data we have presented provide unequivocal evidence that the Tijeras fault was active ca. 32 Ma, so that faulting initiated well before the Miocene. Third, we have presented evidence for right-lateral strike-slip motion that was collected from the damage zone of the Tijeras fault.

Our minor fault data are consistent with left-lateral strike-slip on the Tijeras–Cañoncito fault system during west-northwest–east-southeast rift-related extension (Fig. 8C). Left-lateral slip associated with rifting is also consistent with 2.4 km of left-lateral separation of range-bounding faults where the fault system intersects the rift (Fig. 1; Grauch et al. 1999). We therefore propose that at least some of the left-lateral slip recorded by the fault system occurred during latest Oligocene to Quaternary development of the Rio Grande rift. Some constraints on the timing of this deformation may be offered by the location of the hinge line east of the Sandia–Manzanita uplift, where late Paleozoic rocks were tilted eastward to accommodate uplift of the mountain blocks. Where this rough hinge line intersects the Tijeras–Cañoncito fault system, Paleozoic rocks are exposed virtually continuously across the fault (Fig. 2). A marked discontinuity in exposure would be expected if 1) significant dip-slip motion had occurred along this portion of the fault either before or after uplift or if 2) substantial strike-slip motion postdated uplift, dated by AFT ages at 16–22 Ma (House et al. 2003). Although the hinge line is not sufficiently sharp to offer a true piercing point, these observations suggest that, at this location, fault motion was largely strike-slip, and much of the separation recorded by range-bounding faults may have been accomplished before uplift of the Sandia and Manzanita mountains 16–22 Ma.

Tectonic implications of thermochronologic data

Comparable AFT dates on both sides of the Tijeras fault (Fig. 10; Table 1) preclude substantial differential vertical displacement in the late Oligocene and early Miocene. Therefore, development of the Monte Largo horst/Tijeras graben fault block occurred either before or after this time. We explore each of these possibilities below, and conclude that vertical displacement occurred before the late Oligocene.

If uplift of the horst *predated* the time of cooling below the closure temperature of apatite, rocks of the *same elevation* on either side of the fault would have similar AFT ages (Fig. 15; Laramide uplift path). The effect of current topographic elevation differences on the AFT dates is probably small because all of the samples were taken within a narrow range of topographic elevations (Table 1). The largest difference in elevation is about 146 m, which will have a negligible effect on AFT ages for denudation rates observed elsewhere along the Rio Grande rift/High Plains margin (Kelley and Chapin 1995).

If uplift of the horst *postdated* the time of cooling below the closure temperature of apatite, rocks of *equal stratigraphic position* on either side of the fault would have similar AFT ages (Fig. 15; Neogene uplift path). The granites on the southeast fault block (ML01, ML02) are about 700 m stratigraphically lower than the Abo siltstone (ML03) on the northwest fault block. The magnitude of the effect of stratigraphic position cannot be determined exactly because the denudation rate for this area during the time of cooling is unknown. However, an estimate of the effect may be calculated by assuming a denudation rate. We begin by considering cooling rates calculated from track length data. Confined track lengths are a sensitive record of thermal history (Gleadow et al. 1986). A range of track lengths develops in any sample because each track forms at a different time and partially anneals to a different extent during the thermal history of a sample. A sample with a simple, rapid cooling history will have a narrow, unimodal distribution of track lengths, whereas a slower, simple cooling history will yield a broader, unimodal track length distribution with the mode skewed toward longer tracks. More complex thermal histories produce more complex distributions (Gleadow et al. 1986; Wagner and Van den Haute 1992).

Confined track lengths measured in apatite from samples ML02 and ML04 are presented in Figure 16. The time-temperature paths that best fit the age and track length data for sample ML02 in the Monte Largo horst using the model of Ketchum et al. (1999) are illustrated in Figure 17. Two models were run: one that did not include any geological constraints (Fig. 17A), and one that allowed for cooling during Laramide deformation and heating during Oligocene intrusive activity (Fig. 17B). Note that the fission-track data are insensitive to the thermal history before approximately 30 Ma, but more tightly constrain the post-30 Ma cooling history. The relatively slow, simple cooling history derived from modeling of the AFT data from the Monte Largo horst (Fig. 17A) suggests that the horst did not experience rapid exhumation in the Neogene. Based on the average cooling rate of 3.5 °C/Ma determined for ML02 and assuming a reasonable range of geothermal gradients (25–35 °C/km) for the Rio Grande rift/High Plains boundary (Reiter et al. 1975), we estimate denudation rates that range from 100–140 m/m.y. If the Monte Largo horst were uplifted after the time of cooling below the closure temperature of apatite at denudation rates of 100–140 m/m.y, then the Abo siltstone (ML03) might record a date that is 5–7 m.y. older than that of Proterozoic rocks on the southeast fault block that are equal in present elevation:

$$(700\text{ m}) \times (1\text{ m.y.}/100\text{ to }140\text{ m}) = 7\text{ to }5\text{ m.y.}$$

The effect of stratigraphic position would thus decrease, rather than increase, the uniformity of AFT ages across the fault zone (Fig. 15). Because the AFT ages are uniform across the Tijeras fault, denudation of the horst most likely predated the late Oligocene. Formation of the Tijeras graben/Monte Largo horst fault block must have postdated deposition of the Upper Cretaceous strata because Upper Cretaceous strata are faulted in the Tijeras graben. Therefore, the likely timing of this differential uplift is constrained between the Late Cretaceous and the middle Oligocene. This timing predates the earliest phase of rift deformation (latest Oligocene to early Miocene; Chapin and Cather 1994).

A variety of geologic data mentioned previously further constrain the timing of this pre-rift deformation: 1) Faults from each of the three groups shown in Figure 8 cut rocks that range from Precambrian to Cretaceous in age. Thus all of the deformation recorded is post-Cretaceous in age. 2) North-side-down movement on the Tijeras–Cañoncito fault system controlled subsidence of the Paleogene Galisteo basin (Abbott et al. 1995). 3) Right-lateral separation of gravity anomalies is not associated with displacement along younger rift-related faults, as is left-lateral separation of aeromagnetic anomalies (compare Heywood 1992 with Grauch 1999 and Grauch et al. 1999). We therefore interpret right-lateral transtension on the Tijeras fault to be Late Cretaceous to early Tertiary, or Laramide, in age.

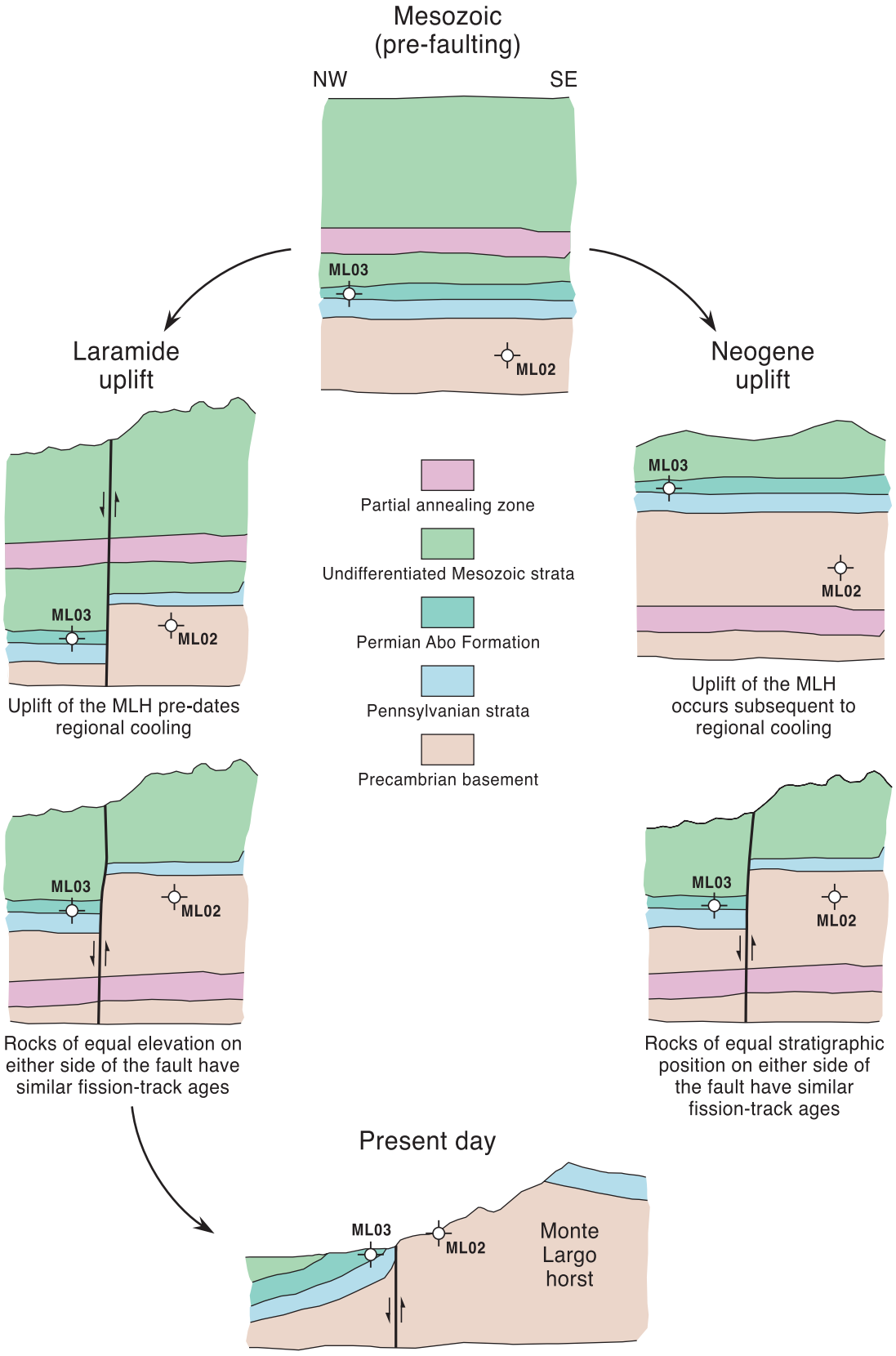

FIGURE 15—Schematic illustration of the effect of the timing of uplift of the Monte Largo horst on fission-track dates. If uplift preceded cooling below the fission-track closure temperature (left path), rocks of equal elevation on either side of the fault would have similar fission-track ages. If uplift post-dated cooling below the fission-track closure temperature (right path), rocks of equal stratigraphic position on either side of the fault would have similar fission-track ages. Laramide uplift (left path) best fits the measured fission-track ages.

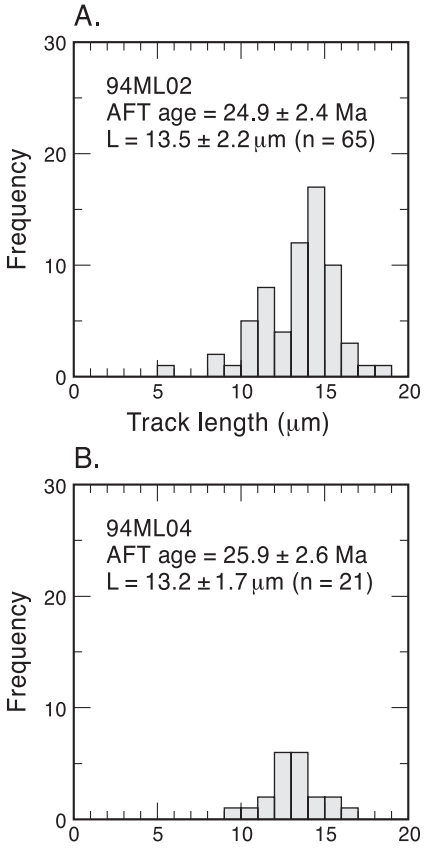

FIGURE 16—Histograms of confined fission-track lengths in apatite. Number of tracks for each cell is corrected to account for track-length bias, which recognizes that longer confined tracks have a higher probability of being etched and revealed than shorter tracks. (**A**) 65 track length measurements from sample ML02. (**B**) 21 track length measurements from sample ML04.

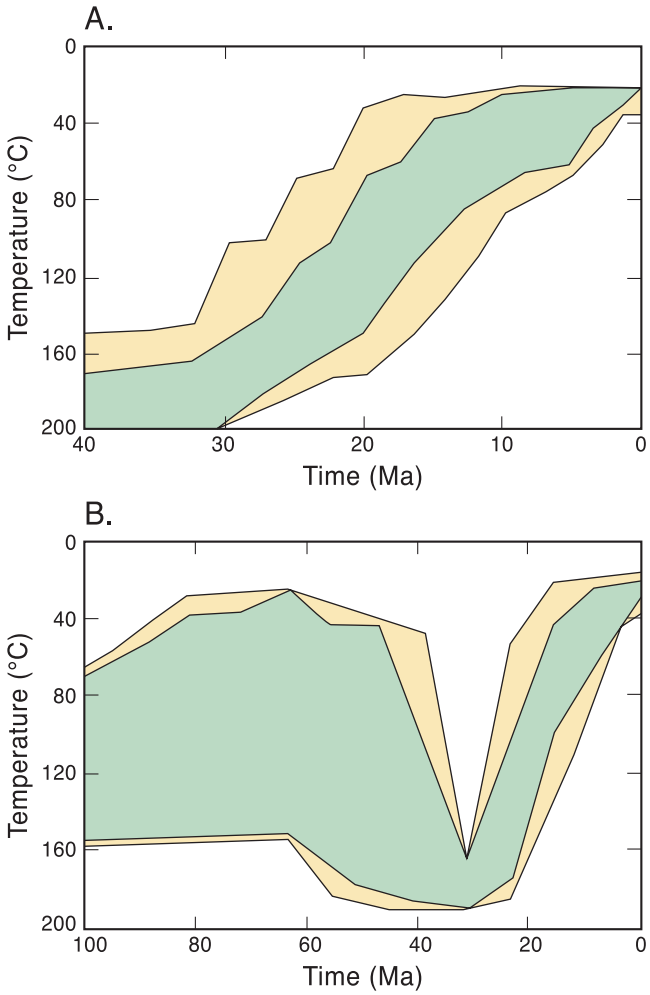

FIGURE 17—Time-temperature inversion model (Ketchum et al. 1999) for sample ML02. Plot shows thermal history solutions compatible with the observed apatite track-length distribution. Green shows solutions passing the Kolmogorov-Smirnov (K-S) test with a probability of > 50% and yellow shows histories passing the K-S criteria at > 5%. (**A**) geological constraints are not included in the model. (**B**) cooling during Laramide deformation and heating during Oligocene intrusive activity are included as model constraints. The solutions illustrate temperatures exceeding 110 °C before early Oligocene time and relatively slow and simple cooling of the Monte Largo horst in the Neogene.

One piece of evidence that seems to contradict this interpretation is the fact that east-northeast-striking faults are also found in the Oligocene porphyritic intrusive rock in the streamcut exposure near Golden (Fig. 4; Abbott and Goodwin 1995). These faults lack kinematic indicators; however, as the porphyritic intrusive rock is post-Laramide in age, it might appear that this is evidence for post-Laramide right-lateral motion. There are three possible explanations for these features. The faults may, in fact, record Oligocene or early Miocene right-lateral motion on the Tijeras–Cañoncito fault system. This hypothesis is supported by Best's (1988) suggestion that Laramide stress orientations persisted until the late Oligocene or early Miocene in the southwestern United States. Alternatively, these faults could be extensions of reactivated Laramide faults that propagated into the porphyritic intrusive rock during the Neogene and/or Quaternary. A third possibility is that when the Tijeras fault served as a transfer fault, accommodating normal motion on one or more north-trending normal faults (cf. Fig. 1), during rift-related deformation, which resulted in local right-lateral slip (as explained earlier, transfer faults typically exhibit variations in sense of slip along their length). These possibilities are not mutually exclusive—all three could be true. Geomorphic evidence for left-lateral strike-slip motion in the Quaternary (Kelson et al. 1999), however, favors the interpretation that these are the extensions of reactivated Laramide-age faults.

Relationship between structures and stresses inferred from minor faults

The existence of a database of paleostress orientations for a large area of northern New Mexico (Erslev 2001) provides an unprecedented opportunity to compare inferred stress with measured strain orientations. As mentioned earlier this also allows an evaluation of deformation partitioning along the fault system. In order to make this comparison it is important to remember that the maximum principal stress is not parallel to the maximum shortening direction for a given fault. Maximum shortening occurs at 45° from the slip direction on a given fault surface; the maximum principal stress is inclined at an angle that varies with the coefficient of friction. For Byerlee friction (Byerlee 1978) this angle is 25–30°. Thus for a purely strike-slip fault the shortening direction will trend 15–20° from the maximum principal stress. For a purely dip-slip fault, the trends will be the same but the plunges differ by 15–20°.

Erslev (2001) documented three compression directions: 1) upper Paleocene to lower Eocene east–east-northeast

compression; 2) northeast–north-northeast compression recorded by faults that cut rocks of Eocene age but not rocks as young as 27 Ma; and 3) mid-Tertiary north-northeast–north compression, recorded locally by faults that cut rocks as young as 24 Ma, interpreted as recording a transition between Laramide and rift-related stress regimes. Our first group of faults (Fig. 8A) is compatible with easterly compression, which is similar to Erslev's first compression orientation. Thus our interpretation of these faults as Laramide in age is consistent with Erslev's (2001) analysis. In addition our assertion that the Tijeras fault accommodated right-lateral transtension is consistent with movement expected during Erslev's documented Laramide stresses, suggesting that partitioning of deformation between the Tijeras–Cañoncito fault system and the surrounding region was not significant.

Our second group of faults (Fig. 8B) is compatible with north-northwest–north-northeast compression, similar to Erslev's (2001) middle Tertiary compression. We note that this stress would be expected to produce left-lateral motion on the Tijera–Cañoncito fault system, consistent with our interpretation. However, as we have noted, there is significant evidence for rift-related left-lateral motion on the fault system southwest of Golden. Thus it is possible that there was a prolonged period of left-lateral strike-slip motion on the Tijeras–Cañoncito fault system that initiated during the transition from Laramide to rift-related stresses and continued into the Quaternary. The second group of faults could include structures developed during any stage in this period.

The exact timing of the period of transition between Laramide shortening and rift-related extension is poorly constrained. Our $^{40}Ar/^{39}Ar$ data from the Ortiz Mountains, together with geologic relationships from previous work (Maynard et al. 1990; Maynard 1995), indicate that deformation producing north-side-down and left-lateral separation occurred ca. 32 Ma. However, we note that this left-lateral separation could have been produced entirely by north-side-down motion, which could result from the latest stages of Laramide right-lateral transtension followed by Neogene rotation of lithologic units. The available data therefore cannot distinguish between two possibilities: 1) Laramide-age right-lateral transtension on the entire fault system could have been followed by local reactivation during the period of transition that Erslev (2001) has documented. Left-lateral and north-side-down motion at ca. 32 Ma in the Ortiz Mountains would then record this transition. The southwestern portion of the fault system subsequently operated as a left-lateral transfer fault into the Quaternary. 2) It is possible that the Laramide fault system was not reactivated until the southwestern portion of the system became a left-lateral transfer fault to accommodate rifting. Left-lateral separation in the Ortiz Mountains could be the result of right-lateral transtension followed by Neogene rotation. If the geometry of the Ortiz graben does indeed reflect left-lateral strike-slip motion, the first option is the most likely. We favor this interpretation.

Our third group of faults does not correspond to any of the stress orientations Erslev (2001) has documented, nor is it consistent with the inferred modern stress field. The northwest extension that these faults record is, however, roughly parallel to the Laramide shortening direction. It is possible that these minor faults reflect unloading of the rocks during exhumation. Fission-track data indicate that exhumation of the fault system occurred ca. 22–26 Ma, at the early stages of rifting. The combination of a vertical maximum principal stress and locked-in strain could have produced this minor fault set at this time.

Tectonic significance of this study

As mentioned in the introduction, the kinematic history of faults in New Mexico is commonly difficult to elucidate. We have offered an approach to sorting out the complex history of one fault zone, using minor fault data, that is consistent with regional paleostress orientations and other geologic information. This approach has allowed us to draw the conclusion that deformation was not strongly partitioned between the Tijeras–Cañoncito fault system and the adjacent region. Damage-zone structures reflect the initiation of right-lateral transtensional faulting during the Laramide orogeny. The fault system was probably reactivated as a left-lateral strike-slip system during the transition between Laramide and rift-related stress fields. The segment of the fault southwest of Golden was subsequently active as a left-lateral transfer fault that accommodated rifting into the Quaternary. Previous work (e.g., Kelson et al. 1999) suggests that the southwestern portion of the fault can still be considered active.

Cather (1992) hypothesized that the Tijeras–Cañoncito fault zone acted as a right-lateral transtensional step in a Laramide-age dextral shear system including the Picuris–Pecos fault to the north and the Montosa fault to the south. We have documented right-lateral transtension on the Tijeras fault at this time. However, the magnitude of extension across the fault system could not have accommodated significant movement on the Picuris–Pecos fault. Subsidence of the northwest fault block is constrained by the maximum thickness of syntectonic sediments of the Diamond Tail and Galisteo Formations adjacent to the fault: 1,300 m. The magnitude of strike-slip accommodated by the heave associated with this subsidence is small relative to the strike-slip recorded by the Picuris–Pecos fault. It is, however, a reasonable order of magnitude with regard to the Laramide-age reverse motion with a dextral component of movement that has been documented on the Montosa fault (Behr et al. 2004 this volume). This suggests that some of the movement on the Picuris–Pecos fault was transferred to other faults in addition to the Tijeras.

Net slip on the fault system (right-lateral Laramide slip minus left-lateral rift-related deformation) resulted in net right-lateral separation of isostatic gravity anomalies of 5.5 km on the east side of the Rio Grande rift (cf. Heywood 1992). Gravity anomalies are offset 13.5 km on the west side of the rift, suggesting that part of the Tijeras–Cañoncito fault system may now be buried beneath the rift. The fact that this net separation is right-lateral may suggest that most of the motion recorded by the fault system took place during the Laramide orogeny. We offer this suggestion with caution, however, as we do not know the origin or orientation of the features producing the gravity anomalies.

Acknowledgments

Thanks to the many colleagues and friends who shared their knowledge of New Mexico geology or assisted in the field: O. Anderson, C. Beck, C. Chapin, R. Colpitts, J. Farren, B. Harrison, J. Hawley, K. Karlstrom, K. Kelson, D. Love, S. Lucas, J. Marcoline, A. Sanford, and T. Sheppler. We thank C. Apache for drafting the tables. Detailed and thoughtful reviews by S. Cather, C. Ferguson, A. Lisenbee, and A. Read improved the paper. J. C. Abbott offers special thanks to A. Cross and M. Zorlu and appreciation of generous financial support from the New Mexico Bureau of Mines and Mineral Resources, the New Mexico Geological Society, the Roswell Geological Society, the Matuszeski Fund of the Graduate Association and the Alumni and Development Office, Anita and Anton Budding, and the New Mexico Tech Graduate Student Research Fund. The fission-track samples were irra-

diated at the Texas A&M Nuclear Science Center under the DOE reactor share program. This paper formed a major part of JCA's M.S. thesis.

References

Abbott, J. C., 1995, Constraints on the deformational history of the Tijeras Cañoncito fault system, north-central New Mexico: Unpublished M.S. thesis, New Mexico Institute of Mining and Technology, 161 pp.

Abbott, J. C., and Goodwin, L. B., 1995, A spectacular exposure of the Tijeras fault, with evidence for Quaternary motion; *in* Bauer, P. W., Kues, B. S., Dunbar, N. W., Karlstrom, K. E., and Harrison, B. (eds.), Geology of the Santa Fe Region: New Mexico Geological Society, Guidebook 46, pp. 117–125.

Abbott, J. C., Cather, S. M., and Goodwin, L. B., 1995, Paleogene synorogenic sedimentation in the Galisteo basin related to the Tijeras–Cañoncito fault system; *in* Bauer, P. W., Kues, B. S., Dunbar, N. W., Karlstrom, K. E., and Harrison, B. (eds.), Geology of the Santa Fe Region: New Mexico Geological Society, Guidebook 46, pp. 271–278.

Allmendinger, R. W., Marrett, R. A., and Cladouhos, T., 1992, FaultKin. Available through http://www.geo.cornell.edu/geology/faculty/RWA/RWA.html, accessed Feb. 10, 2004.

Bachman, G. O., and Mehnert, H. H., 1978, New K-Ar dates and the late Pliocene to Holocene geomorphic history of the central Rio Grande region, New Mexico: Geological Society of America, Bulletin, v. 89, no. 2, pp. 283–292.

Beck, W. C., and Chapin, C. E., 1994, Structural and tectonic evolution of the Joyita Hills, central New Mexico—implications of basement control on Rio Grande rift; *in* Keller, G. R., and Cather, S. M. (eds.), Basins of the Rio Grande rift—structure, stratigraphy, and tectonic setting: Geological Society of America, Special Paper 291, pp. 187–205.

Behr, R. A., Goodwin, L. B., and Kelley, S. A., 2004 this volume, Structural and thermochronological constraints on the movement history of the Montosa fault, New Mexico; *in* Cather, S. M, McIntosh, W. C., and Kelley, S. A. (eds.) Tectonics, geochronology, and volcanism in the Southern Rocky Mountains and Rio Grande rift: New Mexico Bureau of Geology and Mineral Resources, Bulletin 160, pp. 139–160.

Best, M. G., 1988, Early Miocene change in direction of least principal stress, southwestern United States—conflicting inferences from dikes and metamorphic core-detachment fault terranes: Tectonics, v. 8, no. 2, pp. 249–259.

Booth, F. O., 1976, Geology of the Galisteo Creek area, Lamy to Cañoncito, Santa Fe County, New Mexico: Unpublished M.S. thesis, Colorado School of Mines, 122 pp.

Bruns, J. J., 1959, Petrology of the Tijeras Greenstone, Bernalillo County, New Mexico: Unpublished M.S. thesis, University of New Mexico, 119 pp.

Byerlee, J. D., 1978, Friction of rock: Pure and Applied Geophysics, v. 116, no. 4-5, pp. 615–626.

Cather, S. M., 1989, Post Laramide tectonic and volcanic transition in west-central New Mexico; *in* Anderson, O. J., Lucas, S. G., Love, D. W., and Cather, S. M. (eds.), Southeastern Colorado Plateau: New Mexico Geological Society, Guidebook 40, pp. 91–97.

Cather, S. M., 1992, Suggested revisions to the Tertiary tectonic history of north-central New Mexico; *in* Lucas, S. G., Kues, B. S., Williamson, T. E., and Hunt, A. P. (eds.), San Juan Basin IV: New Mexico Geological Society, Guidebook 43, pp. 109–122.

Cather, S. M., 1999, Implications of Jurassic, Cretaceous, and Proterozoic piercing lines for Laramide oblique-slip faulting in New Mexico and rotation of the Colorado Plateau: Geological Society of America, Bulletin, v. 111, no. 6, pp. 849–868.

Chapin, C. E., and Cather, S. M., 1981, Eocene tectonics and sedimentation in the Colorado Plateau–Rocky Mountain area: Arizona Geological Society, Digest, v. 14, pp. 173–198.

Chapin, C. E., and Cather, S. M., 1994, Tectonic setting of the axial basins of the northern and central Rio Grande rift; *in* Keller, G. R., and Cather, S. M. (eds.), Basins of the Rio Grande rift—structure, stratigraphy, and tectonic setting: Geological Society of America, Special Paper 291, pp. 5–25.

Chester, F. M. and Logan, J. M., 1987, Composite planar fabric of gouge from the Punchbowl fault, California: Journal of Structural Geology, v. 9, no. 5-6, pp. 621–634.

Condie, K. C., 1982, Plate-tectonics model for Proterozoic continental accretion in the southwestern United States: Geology, v. 10, no. 1, pp. 37–42.

Connolly, J. R., 1981, Geology of the Precambrian rocks of Tijeras Canyon, Bernalillo County, New Mexico: Unpublished M.S. thesis, University of New Mexico, 147 pp.

Connolly, J. R., 1982, Structure and metamorphism in the Precambrian Cibola gneiss and Tijeras greenstone, Bernalillo County, New Mexico; *in* Wells, S. G., Grambling, J. A., and Callender, J. F. (eds.), Albuquerque country II: New Mexico Geological Society, Guidebook 33, pp. 197–202.

Cordell, L., 1978, Regional geophysical setting of the Rio Grande rift: Geological Society of America, Bulletin, v. 89, pp. 1073–1090.

Deino, A. and Potts, R., 1990, Single-crystal $^{40}Ar/^{39}Ar$ dating of the Olorgesailie Formation, Southern Kenya rift: Journal of Geophysical Research, v. 95, pp. 8453–8470.

Deino, A., and Potts, R., 1992, Age-probability spectra for examination of single-crystal $^{40}Ar/^{39}Ar$ dating results—examples from Olorgesailie, Southern Kenya rift: Quaternary International, v. 13/14, pp. 47–53.

Erslev, E. A., 2001, Multi-stage, multi-directional Tertiary shortening and compression in north-central New Mexico: Geological Society of America, Bulletin, v. 113, no. 1, pp. 63–74.

Ferguson, C. A., 1999, Structural geometry, kinematics, and timing of deformation and magmatism in the Tijeras fold-belt—implications for Laramide through mid-Tertiary tectonic evolution of the southern Rockies (abs.): Geological Society of America, Abstracts with Programs, v.3 1, p. A-187.

Ferguson, C. A., Timmons, J. M., Pazzaglia, F. J., Karlstrom, K. E., Osburn, G. R., and Bauer, P. W., 1999, Geology of Sandia Park quadrangle, Bernalillo and Sandoval Counties, New Mexico: New Mexico Bureau of Mines and Mineral Resources, Open-file Geologic Map OF-GM 1, scale 1:24,000.

Fleck, R. J., Sutter, J. F., and Elliot, D. H., 1977, Interpretation of discordant $^{40}Ar/^{39}Ar$ age spectra of Mesozoic tholeiites from Antarctica: Geochimica et Cosmochimica Acta, v. 41, no. 4, pp. 15–32.

Galbraith, R .F., 1981, On statistical models for fission track counts: Mathematical Geology, v. 13, pp. 471–478.

Galbraith, R. F., 1988, Graphical display of estimates having differing standard errors: Technometrics, v. 30, no. 3, pp. 271–281.

Galbraith, R. F., and Laslett, G. M., 1985, Some remarks on statistical estimation in fission-track dating: Nuclear Tracks, v. 10, no. 3, pp. 361–363.

Galbraith, R. F., and Laslett, G. M., 1993, Statistical models for mixed fission track ages: Nuclear Tracks and Radiation Measurement, v. 21, no. 4, pp. 459–470.

Ghisetti, F., 2000, Slip partitioning and deformation cycles close to major faults in southern California—evidence from small-scale faults: Tectonics v. 19, no 1, pp. 25–43.

Gibbons, J. F., 1990, Tectonic disruption of Tijeras Canyon drainage (abs.): New Mexico Geology, v. 12, no. 4, p. 93.

Gleadow, A. J. W., Duddy, I. R., Green, P. F., and Hegarty, K. A., 1986, Fission track lengths in the apatite annealing zone and the interpretation of mixed ages: Earth and Planetary Science Letters, v. 78, no. 2-3, pp. 245–254.

GRAM, Inc. and William Lettis & Associates, Inc., 1995, Conceptual geological model of the Sandia National Laboratories and Kirtland Air Force Base: Technical Report submitted to the Site-wide Hydrologic Characterization Project, Organization 7584, Environmental Restoration Project, Sandia Laboratories, Albuquerque, New Mexico, 2 volumes, various pagination.

Grauch, V. J. S., 1999, Principal features of high-resolution aeromagnetic data collected near Albuquerque, New Mexico; *in* Pazzaglia, F. J., and Lucas, S. G. (eds.), Albuquerque geology: New Mexico Geological Society, Guidebook 50, pp. 115–119.

Grauch, V. J. S., Gillespie, C. L., and Keller, G. R., 1999, Discussion of new gravity maps for the Albuquerque basin area; *in* Pazzaglia, F. J., and Lucas, S. G. (eds.), Albuquerque geology: New Mexico Geological Society, Guidebook 50, pp. 119–124.

Green, P. F., 1985, A comparison of zeta calibration baselines in zircon, sphene, and apatite: Chemical Geology, Isotope Geoscience Section, v. 58, pp. 1–22.

Heywood, C. E., 1992, Isostatic residual gravity anomalies of New Mexico: U.S. Geological Survey, Water Resources Investigations Report WRI-91-4065, 27 pp.

House, M. A., Kelley, S. A., and Roy, M., 2003, Refining the footwall

cooling history of a rift flank uplift, Rio Grande rift, New Mexico: Tectonics, v. 22, no 5, 18 pp.

Hurford, A. J., 1986, Cooling and uplift patterns in the Lepontine Alps, south central Switzerland and an age of vertical movement on the Insubric fault line: Contributions to Mineralogy and Petrology, v. 92, no. 4, pp. 413–427.

Hurford, A. J., and Green, P. F., 1983, The zeta age calibration of fission-track dating: Isotope Geoscience, v. 1, no. 4, pp. 285–317.

Hurford, A. J., Fitch, F. J., and Clarke, A., 1984, Resolution of the age structure of the detrital zircon populations of two Lower Cretaceous sandstones from the Weald of England by fission track dating: Geological Magazine, v. 121, no. 4, pp. 269–296.

Ilg, B., Bauer, P. W., Ralser, S., Rogers, J., and Kelley, S., 1997, Geology of the Glorieta 7.5-min quadrangle, Santa Fe County, New Mexico: New Mexico Bureau of Mines and Mineral Resources, Open-file Geologic Map OG-FM-11, scale 1:12,000.

Karlstrom, K. E., Connell, S. D., Ferguson, C. A., Read, A. S., Osburn, G., Kirbey, E., Abbott, J. C., Hitchcock, C., Kelson, K. I., Noller, J., Sawyer, T., Ralser, S., Love, D. W., Nyman, M., and Bauer, P. W., 1994, Geology of the Tijeras 7.5-min quadrangle, Bernalillo County, New Mexico: New Mexico Bureau of Geology and Mineral Resurces, Open-file Geologic Map OF-GM 4, scale 1:24,000.

Kay, B. D., 1986, Vein and breccia gold mineralization and associated igneous rocks at the Ortiz mine, New Mexico, U.S.A.: Unpublished M.S. thesis, Colorado School of Mines, 179 pp.

Kelley, S. A., and Chapin, C. E., 1995, Apatite fission-track thermochronology of southern Rocky Mountains–Rio Grande rift–western High Plains provinces; *in* Bauer, P. W., Kues, B. S., Dunbar, N. W., Karlstrom, K. E., and Harrison, B. (eds.), Geology of the Santa Fe region: New Mexico Geological Society, Guidebook 46, pp. 87–96.

Kelley, S. A., and Chapin, C. E., 2004 this volume, Denudational history and internal structure of the Front Range and Wet Mountains, Colorado, based on apatite fission-track thermochronology; *in* Cather, S. M., McIntosh, W. C., and Kelley, S. A. (eds.), Tectonics, geochronology, and volcanism in the Southern Rocky Mountains and Rio Grande rift: New Mexico Bureau of Geology and Mineral Resources, Bulletin 160, pp. 41–78.

Kelley, S. A., and I. J. Duncan, 1984, Tectonic history of the northern Rio Grande rift derived from apatite fission-track geochronology; *in* Baldridge, W. S., Dickerson, P. W., Riecker, R. E., and Zidek, J. (eds.), Rio Grande rift, northern New Mexico: New Mexico Geological Society, Guidebook 35, pp. 67– 73.

Kelley, S. A., and Duncan, I. J., 1986, Late Cretaceous to middle Tertiary tectonic history of the northern Rio Grande rift: Journal of Geophysical Research, v. 91, no. 6B, pp. 6246–6262.

Kelley, S. A., Chapin, C. E., and Corrigan, J., 1992, Late Mesozoic to Cenozoic cooling histories of the flanks of the northern and central Rio Grande rift, Colorado and New Mexico: New Mexico Bureau of Mines and Mineral Resources Bulletin 145, 40 pp.

Kelley, V. C., 1954, Tectonic map of a part of the upper Rio Grande area, New Mexico: U.S. Geological Survey, Oil and Gas Investigation Map OM-157, scale 1:190,080.

Kelley, V. C., and Northrop, S. A., 1975, Geology of Sandia Mountains and vicinity, New Mexico: New Mexico Bureau of Mines and Mineral Resources, Memoir 29, 136 pp.

Kelson, K. I., Hitchcock, C. S., and Harrison, J. B. J., 1999, Paleoseismology of the Tijeras fault near Golden, New Mexico: *in* Pazzaglia, F. J., and Lucas, S. G. (eds.), Albuquerque geology: New Mexico Geological Society, Guidebook 50, pp. 201–209.

Ketchum, R. A., Donelick, R. A, and Carlson, W. D., 1999, Variability of apatite fission-track annealing kinetics, III. extrapolation to geological time scales: American Mineralogist, v. 84, pp. 1235–1255.

Kirby, E., Karlstrom, K. E., Andronicos, C. L., and Dallmeyer, R. D., 1995a, Tectonic setting of the Sandia pluton—an orogenic 1.4 Ga granite in New Mexico: Tectonics, v. 14, no. 1, pp. 185–201.

Kirby, E., Karlstrom, K. E., and Andronicos, C. L., 1995b, Structural and thermal setting during emplacement of the Sandia pluton; *in* Bauer, P. W., Kues, B. S., Dunbar, N. W., Karlstrom, K. E., and Harrison, B. (eds.), Geology of the Santa Fe region: New Mexico Geological Society, Guidebook 46, pp. 219–226.

Laslett, G. M., Kendall, W. S., Gleadow, A. J. W., and Duddy, I. R., 1982, Bias in measurement of fission-track length distribution: Nuclear Tracks, v. 6, no. 2-3, pp. 79–85.

Lisenbee, A. L. and Woodward, L. E., 1995, Tijeras–Cañoncito accommodation zone, Rio Grande rift, New Mexico (abs.): Geological Society of America, Abstracts with Programs, Rocky Mountain Section, v. 27, no. 4, p. 43.

Lisenbee, A. L., Woodward, L. A., and Connolly, J. R., 1979, Tijeras–Cañoncito fault system—a major zone of recurrent movement in north-central New Mexico; *in* Ingersoll, R. V., Woodward, L. A. and James, H. L. (eds.), Santa Fe country: New Mexico Geological Society, Guidebook 30, pp. 89–99.

Machette, M. N., 1982, Quaternary and Pliocene faults in the La Jencia and southern part of the Albuquerque–Belen Basins, New Mexico—evidence of fault history from fault scarp morphology and Quaternary geology; *in* Wells, S. G., Grambling, J. A., and Callender, J. F. (eds.), Albuquerque country II: New Mexico Geological Society, Guidebook 33, pp. 161–169.

Machette, M. N., Personius, S. F., Kelson, K. I, Dart, R. L., and Haller, K. M., 1998, Map and data for Quaternary faults in New Mexico: U.S. Geological Survey, Open-file Report 98-521, 1 plate, scale 1:750,000 scale.

Maldonado, F., Connell, S. D., Love, D. W., Grauch, V. J. S ., Slate, J. L., McIntosh, W. C., Jackson, P. B., and Byers, F. M., Jr., 1999, Neogene geology of the Isleta Reservation and vicinity, Albuquerque Basin, New Mexico; *in* Pazzaglia, F. J., and Lucas, S. G. (eds.) Albuquerque geology: New Mexico Geological Society, Guidebook 50, pp. 175–188.

Marrett, R., and Allmendinger, R. W., 1990, Kinematic analysis of fault slip-data: Journal of Structural Geology, v.12, no. 43, pp. 973–986.

Mawer, C. K., Grambling, J. A., and Vernon, R. H., 1989, Syntectonic nature of the 1.45 Ga Sandia pluton, New Mexico (abs.): Geological Society of America, Abstracts with Programs, v. 21, no. 6, p. 215.

May, S. J., and Russell, L. R., 1994, Thickness of the syn-rift Santa Fe Group in the Albuquerque Basin and its relation to structural style; *in* Keller, G. R., and Cather, S. M. (eds.), Basins of the Rio Grande rift—structure, stratigraphy, and tectonic setting: Geological Society of America, Special Paper 291, pp. 113–123.

Maynard, S. R., 1995, Gold mineralization associated with mid-Tertiary magmatism and tectonism, Ortiz Mountains, Santa Fe County, New Mexico; *in* Bauer, P. W., Kues, B. S., Dunbar, N. W., Karlstrom, K. E, and Harrison, B. (eds.), Geology of the Santa Fe region: New Mexico Geological Society, Guidebook 46, pp. 161–166.

Maynard, S. R., Nelsen, C. J., Martin, K. W., and Schutz, J. L., 1990, Geology and gold mineralization of the Ortiz Mountains, Santa Fe County, New Mexico: Mining Engineering, v. 42, no. 8, pp. 1007–1011.

Maynard, S. R., Woodward, L. A., and Giles, D. L., 1991, Tectonics, intrusive rocks, and mineralization of the San Pedro–Ortiz porphyry belt, north-central New Mexico: New Mexico Bureau of Mines and Mineral Resources, Bulletin 137, pp. 57–69.

Miller, J. P., Montgomery, A., and Sutherland, P. K., 1963, Geology of part of the southern Sangre de Cristo Mountains, New Mexico: New Mexico Bureau of Mines and Mineral Resources, Memoir 11, 106 pp.

Mount, V. S and Suppe, J., 1987, Present-day stress orientations adjacent to active strike-slip faults—California and Sumatra: Journal of Geophysical Research, v. 97, no. 8, pp. 11,995–12,013.

Nelson, B. K. and DePaolo, D. J., 1984, Origin of Precambrian metavolcanic rocks from New Mexico, Colorado, and Wyoming, and the isotopic evolution of Proterozoic mantle (abs.): Geological Society of America, Abstracts with Programs, v. 16, no. 4, pp. 249.

Petit, J. P., 1987, Criteria for the sense of movement on fault surfaces in brittle rocks: Journal of Structural Geology, v. 9, no. 5-6, pp. 597–608.

Ramberg, I. B., Cook, F. A., and Smithson, S. B., 1978, Structure of the Rio Grande rift in southern New Mexico and West Texas based on gravity interpretation: Geological Society of America, Bulletin, v. 89, no. 1, pp. 107–123.

Reiter, M., Edwards, C. L., Hartman, H., Weidman, C., 1975, Terrestrial heat flow along the Rio Grande rift, New Mexico and southern Colorado: Geological Society of America, Bulletin, v. 86, no. 6, pp. 811–818.

Riedel, W., 1929, Zur Mechanik geologischer Brucherrscheinungen: Centralbl. F. Mineral. Geol. U. Pal. 1929 B, pp. 354–368.

Russell, L. R., and Snelson, S., 1990, Structural style and tectonic

evolution of the Albuquerque Basin segment of the Rio Grande rift, in Pinet, B., and Bois, C. (eds.), The potential of deep seismic profiling for hydrocarbon exploration: Editions Technip, Paris, pp. 175–207.

Russell, L. R., and Snelson, S., 1994, Structure and tectonics of the Albuquerque Basin segment of the Rio Grande rift—insights from seismic reflection data; *in* Keller, G. R., and Cather, S. M. (eds.), Basins of the Rio Grande rift—structure, stratigraphy, and tectonic setting: Geological Society of America, Special Paper 291, pp. 83–112.

Samson, S. D., and, Alexander, E. C., Jr., 1987. Calibration of the interlaboratory $^{40}Ar/^{39}Ar$ dating standard, Mmhb-1: Chemical Geology, v. 66, no. 1-2, pp. 27–34.

Sanford, A. R., Jaksha, L. H., and Cash, D. J., 1991, Seismicity of the Rio Grande rift in New Mexico; *in* Slemmons, D. B., Engdahl, E. R., Zoback, M. D., and Blackwell, D. D. (eds.), Neotectonics of North America: Geological Society of America, Decade Map, v. 1, pp. 229–244.

Sauer, R. R., 1999, Petrochemistry and geochronology of plutons relative to tectonics in the San Pedro–Ortiz porphyry belt, New Mexico: Unpublished M.S. thesis, University of Colorado, 115 pp.

Starkey, J., 1977, The contouring of orientation data represented in spherical projection: Canadian Journal of Earth Sciences, v. 14, no. 2, p. 268–277.

Stearns, C. E., 1953, Tertiary geology of the Galisteo–Tonque area, north-central New Mexico: Geological Society of America, Bulletin, v. 64, no. 4, pp. 459–508.

Steiger, R. H., and Jäger, E., 1977, Subcommission on geochronology—convention on the use of decay constants in geo- and cosmochronology: Earth and Planetary Science Letters, v. 36, pp. 359–362.

Tavarnelli, E., 1998, Tectonic evolution of the northern Salient Block, California. USA—Paleogene to Recent shortening in a transform fault-bounded continental fragment; *in* Holdsworth, R. E., Strachan, R. A., and Dewey, J. F. (eds), Continental transpressional and transtensional tectonics: Geological Society, London, Special Publications, v. 135, pp. 107–118.

Taylor, J. R., 1982. An introduction to error analysis—the study of uncertainties in physical measurements. University Science Books, Mill Valley, Calif., 270 pp.

Tchalenko, J. S., 1970, Similarities between shear zones of different magnitudes: Geological Society of America, Bulletin, v. 81, no. 6, pp. 1625–1640.

Teyssier, C., Tikoff, B., and Markley, M., 1995, Oblique plate motion and continental tectonics: Geology, v. 23, no. 5, pp. 447–450.

Timmons, J. M., Karlstrom, K. E., and Kirby, E., 1995, Geology of the Monte Largo Hills area, New Mexico—structural and metamorphic study of the eastern aureole of the Sandia Pluton; *in* Bauer, P. W., Kues, B. S., Dunbar, N. W., Karlstrom, K. W., and Harrison, B. (eds.), Geology of the Santa Fe region: New Mexico Geological Society, Guidebook 46, pp. 227–232.

Vernon, R. H., 1986, K-feldspar megacrysts in granites—phenocrysts, not porphyroblasts: Earth Science Reviews, v. 23, no. 1, pp. 1–63.

Wagner, G. and van den Haute, P., 1992, Fission track dating: Kluwer Academic Publishers, Dordrecht, The Netherlands, 285 pp.

Wilson, J. E., 1999, Microfracture fabric of the Punchbowl fault zone, San Andreas system, California: Unpublished M.S. Thesis, Texas A&M University, 125 pp.

Woodward, L. A., 1984, Basement control of Tertiary intrusions and associated mineral deposits along Tijeras–Cañoncito fault system, New Mexico: Geology, v. 12, no. 9, pp. 531–533.

Yamada, R., Tagami, T., Nishimura, S., and Ito, H., 1995, Annealing kinetics of fission tracks in zircon—an experimental study: Chemical Geology, Isotope Geoscience Section, v. 122, no. 1-4, pp. 249–258.

York, D., 1969. Least squares fitting of a straight line with correlated errors: Earth and Planetary Science Letters, v. 5, no. 5, pp. 320–324.

Zoback, M. D., Zoback, M. L., Mount, V. S, Suppe, J., Eaton, J. P., Healy, J. H., Oppenheimer, D., Reasenberg, P., Jones, L., Raleigh, C. B., Wong, I. G., Scotti, O., and Wentworth, C., 1987, New evidence on the state of stress of the San Andreas fault system: Science, v. 238, pp.1105–1111.